

## On the Fraction of X-ray Weak Quasars from the Sloan Digital Sky Survey

XINGTING PU,<sup>1,2</sup> B. LUO,<sup>1,3,4</sup> W. N. BRANDT,<sup>5,6,7</sup> JOHN D. TIMLIN,<sup>5</sup> HEZHEN LIU,<sup>1,3,4</sup> Q. NI,<sup>5,6</sup> AND JIANFENG WU<sup>8</sup>

<sup>1</sup>*School of Astronomy and Space Science, Nanjing University, Nanjing, Jiangsu 210093, China; bluo@nju.edu.cn*

<sup>2</sup>*College of Science, Nanjing Forestry University, Nanjing, Jiangsu 210037, China*

<sup>3</sup>*Key Laboratory of Modern Astronomy and Astrophysics (Nanjing University), Ministry of Education, Nanjing, Jiangsu 210093, China*

<sup>4</sup>*Collaborative Innovation Center of Modern Astronomy and Space Exploration, Nanjing, Jiangsu 210093, China*

<sup>5</sup>*Department of Astronomy & Astrophysics, 525 Davey Lab, The Pennsylvania State University, University Park, PA 16802, USA*

<sup>6</sup>*Institute for Gravitation and the Cosmos, The Pennsylvania State University, University Park, PA 16802, USA*

<sup>7</sup>*Department of Physics, 104 Davey Lab, The Pennsylvania State University, University Park, PA 16802, USA*

<sup>8</sup>*Department of Astronomy, Xiamen University, Xiamen, Fujian 361005, China*

### ABSTRACT

We investigate systematically the X-ray emission from type 1 quasars using a sample of 1825 Sloan Digital Sky Survey (SDSS) non-broad absorption line (non-BAL) quasars with *Chandra* archival observations. A significant correlation is found between the X-ray-to-optical power-law slope parameter ( $\alpha_{\text{OX}}$ ) and the 2500 Å monochromatic luminosity ( $L_{2500 \text{ \AA}}$ ), and the X-ray weakness of a quasar is assessed via the deviation of its  $\alpha_{\text{OX}}$  value from that expected from this relation. We demonstrate the existence of a population of non-BAL X-ray weak quasars, and the fractions of quasars that are X-ray weak by factors of  $\geq 6$  and  $\geq 10$  are  $5.8 \pm 0.7\%$  and  $2.7 \pm 0.5\%$ , respectively. We classify the X-ray weak quasars (X-ray weak by factors of  $\geq 6$ ) into three categories based on their optical spectral features: weak emission-line quasars (WLQs; C IV REW  $< 16 \text{ \AA}$ ), red quasars ( $\Delta(g-i) > 0.2$ ), and unclassified X-ray weak quasars. The X-ray weak fraction of  $35^{+12}_{-9}\%$  within the WLQ population is significantly higher than that within non-WLQs, confirming previous findings that WLQs represent one population of X-ray weak quasars. The X-ray weak fraction of  $13^{+5}_{-3}\%$  within the red quasar population is also considerably higher than that within the normal quasar population. The unclassified X-ray weak quasars do not have unusual optical spectral features, and their X-ray weakness may be mainly related to quasar X-ray variability.

*Keywords:* galaxies: active – galaxies: nuclei – quasars: emission lines – X-rays: galaxies

### 1. INTRODUCTION

X-ray emission is an ubiquitous property of active galactic nuclei (AGNs). Extragalactic X-ray surveys with *Chandra* and *XMM-Newton* have provided a quite complete understanding of the distant AGN population (see Brandt & Alexander 2015 for a review). AGN X-ray emission has been found to be strongly correlated with the optical/UV emission (e.g., Avni & Tananbaum 1982; Avni & Tananbaum 1986). It is believed that AGN optical/UV photons are emitted from the accretion disk, and X-ray continuum emission arises from inverse Compton scattering of these optical/UV photons in a hot accretion-disk “corona” (e.g., Galeev et al. 1979; Reynolds & Nowak 2003; Jiang et al. 2014). The X-ray-to-optical power-law slope parameter  $\alpha_{\text{OX}}$ , conventionally defined as  $\alpha_{\text{OX}} = 0.3838 \log(L_{2 \text{ keV}}/L_{2500 \text{ \AA}})$  (Tananbaum et al.

1979),<sup>1</sup> is commonly used to quantify the ratio between the X-ray and optical/UV luminosity of AGNs. Studies of the X-ray and optical/UV emission of large AGN samples have established a significant  $\alpha_{\text{OX}}-L_{2500 \text{ \AA}}$  anti-correlation spanning a broad range in  $L_{2500 \text{ \AA}}$  and redshift (e.g., Vignali et al. 2003; Strateva et al. 2005; Steffen et al. 2006; Just et al. 2007; Lusso et al. 2010; Lusso & Risaliti 2016; Chiaraluce et al. 2018), providing fundamental constraints on disk-corona models for AGNs.

The empirical  $\alpha_{\text{OX}}-L_{2500 \text{ \AA}}$  relation also allows identification of unusual X-ray weak AGNs (especially X-ray weak type 1 quasars), showing X-ray emission significantly weaker than that expected from the  $\alpha_{\text{OX}}-L_{2500 \text{ \AA}}$  relation. The nearby ( $z = 0.192$ ) narrow-line type 1 quasar PHL 1811 is the best-studied example of this class (Leighly et al. 2007b). The X-ray luminosity of

<sup>1</sup>  $L_{2 \text{ keV}}$  and  $L_{2500 \text{ \AA}}$  represent the rest-frame 2 keV and 2500 Å monochromatic luminosities, respectively.

PHL 1811 is a factor of  $\sim 30$ – $100$  times weaker than that expected from the  $\alpha_{\text{OX}}-L_{2500 \text{ \AA}}$  relation. The steep X-ray spectrum (with photon index  $\Gamma = 2.3 \pm 0.1$ ), lack of evidence for intrinsic X-ray and UV absorption, and short-term X-ray flux variability by a factor of  $\sim 5$  strongly suggest that PHL 1811 is intrinsically X-ray weak (Leighly et al. 2007b). The optical/UV line emission of PHL 1811 is also unusual (e.g., no forbidden or semiforbidden lines, very strong Fe II and Fe III, unusual very low-ionization lines, and very weak high-ionization lines; see Leighly et al. 2007a). Its C IV emission line is blueshifted and asymmetric, and it has a rest-frame equivalent width (REW) of only  $6.6 \text{ \AA}$ , about 5 times smaller than that in the composite quasar spectrum (Vanden Berk et al. 2001).

Except for a few candidates for intrinsically X-ray weak quasars (e.g., Gallagher et al. 2001; Wu et al. 2011; Luo et al. 2013, 2014; Liu et al. 2018) like PHL 1811, X-ray weakness in type 1 quasars is generally ascribed to absorption. Broad absorption line (BAL) quasars are well known to be X-ray weak compared to quasars with normal optical/UV spectra (e.g., Green & Mathur 1996; Brandt et al. 2000; Gallagher et al. 2006). Approximately one in every six optically selected quasars shows BALs in its rest-frame UV spectra (e.g., Reichard et al. 2003; Gibson et al. 2009a). Spectroscopic X-ray studies have found that BAL quasars typically have underlying X-ray continua similar to those of normal quasars (Gallagher et al. 2002) and the X-ray weakest BAL quasars tend to have the hardest X-ray spectra (Gallagher et al. 2006), suggesting that the X-ray weakness in BAL quasars is primarily due to absorption.

There is a small population of weak emission-line quasars (WLQs; e.g., Shemmer et al. 2009; Diamond-Stanic et al. 2009; Plotkin et al. 2010a; Laor & Davis 2011; Wu et al. 2012) that are known often to show weak X-ray emission. They have broad UV emission lines (e.g., C IV  $\lambda 1549$ ) that are significantly weaker than those of normal quasars. Studies of large samples of this class of objects have found that a large fraction ( $\gtrsim 50\%$ ) of WLQs are X-ray weak (Wu et al. 2012; Luo et al. 2015; Ni et al. 2018). The small effective power-law photon index ( $\Gamma_{\text{eff}} \approx 1.2$ ) measured from X-ray stacking analyses indicates that the X-ray weak WLQs are on average likely X-ray absorbed (e.g., with  $N_{\text{H}} \approx 9 \times 10^{23} \text{ cm}^{-2}$ ; Luo et al. 2015).

Few studies have investigated systematically the populations of X-ray weak quasars. Gibson et al. (2008a) analyzed the X-ray and UV properties of 536 Sloan Digital Sky Survey (SDSS; York et al. 2000) quasars, including 315 with *Chandra* coverage and 221 with *XMM-Newton* coverage. Based on 139 RQ non-BAL quasars in sample B of Gibson et al. (2008a), their results showed that X-ray weak quasars are rare. Limited by their sample size, however, they only measured upper limits on

the fraction of type 1 quasars with a given factor of X-ray weakness (Figure 5 of Gibson et al. 2008a).

Motivated by the significantly increased numbers of SDSS quasars and *Chandra* observations since the Gibson et al. (2008a) work, we present here a systematic and uniform X-ray study of 1825 quasars with *Chandra* coverage, which are drawn from the SDSS Seventh Data Release (DR7; Abazajian et al. 2009) and Tenth Data Release (DR10; Ahn et al. 2014). Using the updated optical/UV and X-ray data, we can not only constrain better the fraction of X-ray weak quasars, but also attempt to classify the causes for their X-ray weakness. Studies of the fraction and nature of these populations of exceptional objects may provide insights into the disk-corona system and nuclear obscuring material for accreting supermassive black holes (SMBHs). We describe our sample selection and X-ray data analysis in Sections 2 and 3, respectively. The results, including the X-ray and optical/UV properties, and the fraction of X-ray weak quasars, are presented in Section 4. In Section 5, we discuss the nature of quasar X-ray weakness. We summarize in Section 6. Throughout this work, we use J2000 coordinates and a cosmology with  $H_0 = 70 \text{ km s}^{-1} \text{ Mpc}^{-1}$ ,  $\Omega_{\text{M}} = 0.3$ , and  $\Omega_{\Lambda} = 0.7$  (e.g., Spergel et al. 2007).

## 2. SAMPLE SELECTION

### 2.1. SDSS and Chandra Archive Selection

The SDSS DR7 quasar catalog (Schneider et al. 2010) contains 105,783 bona fide quasars in the redshift range  $0.065 < z < 5.460$  that have luminosities brighter than  $M_i = -22.0$  and have at least one broad emission line with the full width at half-maximum (FWHM) larger than  $1000 \text{ km s}^{-1}$  or have interesting/complex absorption features. The SDSS DR10 quasar catalog (Pâris et al. 2014) contains 166,583 Baryon Oscillation Spectroscopic Survey (BOSS) objects that have luminosities  $M_i < -20.5$  and either have at least one emission line with the FWHM larger than  $500 \text{ km s}^{-1}$  or have interesting/complex absorption features.

We selected DR7 and DR10 quasars in the redshift range  $1.700 < z < 2.700$ . The lower limit on the redshift ensures that the full velocity range up to  $29,000 \text{ km s}^{-1}$  shortward of the C IV  $\lambda 1549$  emission line is redshifted into the SDSS and BOSS spectra, allowing unambiguous identification of BAL quasars from their broad C IV absorption. The upper limit on the redshift ensures that the effective wavelengths (rest-frame  $\gtrsim 2000 \text{ \AA}$ ) of the absolute i-band magnitudes, which are extrapolated to derive the rest-frame  $2500 \text{ \AA}$  flux densities (Section 2.3 below), do not deviate much from  $2500 \text{ \AA}$ . We then searched the *Chandra* archive to find ACIS (Advanced CCD Imaging Spectrometer; Garmire et al. 2003) observations (with no gratings) that were public as of 2016 July 1 and have pointing positions within  $17'$  of the selected sources. We used the FIND\_CHANDRA\_OBSID script in *Chandra* Interactive Analysis of Observations

(CIAO)<sup>2</sup> to check if these sources are actually covered by *Chandra*,<sup>3</sup> resulting in a parent sample of 2475 SDSS quasars with 1472 *Chandra* observation IDs.<sup>4</sup>

## 2.2. Excluding BAL Quasars

It is necessary to exclude BAL quasars to avoid quasars with possible strong X-ray absorption. The Shen et al. (2011) DR7 quasar catalog lists a `BAL_flag` parameter indicating the identification of BAL quasars. This parameter flags both the objects in the SDSS Fifth Data Release (DR5) BAL quasar catalog (Gibson et al. 2009a) and the visually confirmed post-DR5 BAL quasars. The Pâris et al. (2014) DR10 quasar catalog lists a `BAL_FLAG_VI` parameter flagging those visually confirmed BAL quasars and also a `BI_CIV` parameter indicating the traditional BAL quasars (Weymann et al. 1991). We consider a DR7 quasar with `BAL_flag` > 0 in the Shen et al. (2011) catalog or a DR10 quasar with `BAL_FLAG_VI` = 1 or `BI_CIV` > 0 in the Pâris et al. (2014) catalog a BAL quasar. In our parent sample, 345 quasars satisfy one or more of these criteria and they were thus excluded.

The BI<sub>0</sub> definition adopted by Gibson et al. (2009a) and the BI definition adopted by Pâris et al. (2014) both apply a conservative absorption trough width threshold of 2000 km s<sup>-1</sup>. This threshold may miss relatively weak BAL features. Therefore, we adopted the absorption index (AI; e.g., Trump et al. 2006) parameter to search for additional BAL quasars. It was computed as

$$\text{AI} \equiv \int_0^{29,000} (1 - f(v))C \, dv, \quad (1)$$

where  $f(v)$  is the continuum-normalized flux density. The value of  $C$  is initially set to zero; it is set to 1 whenever  $f(v)$  has been continuously less than 0.9 for more than 1000 km s<sup>-1</sup>. A sample object with AI > 0 is also considered a BAL quasar.

We fitted the SDSS and BOSS spectra of our sample quasars following the method of Gibson et al. (2008b), which we summarize briefly here. For each sample quasar, we corrected its spectrum for Galactic extinction using the reddening curve of Cardelli et al. (1989) and O'Donnell (1994). The continuum was fitted by a power law with Small Magellanic Cloud (SMC) reddening (Pei 1992); the continuum regions were selected to be rest-frame 1250–1350, 1600–1800, 1950–2050, 2150–2250, and 2950–3700 Å, which are free from strong emission and absorption features. We iteratively fitted the

continuum regions with a  $3\sigma$  clipping method (i.e., spectral bins that deviate from the continuum model by more than  $3\sigma$  were ignored at each iteration, with  $\sigma$  being the spectral error). The continuum was determined using the three best-fit parameters: power-law normalization, spectral index  $\alpha_\lambda$ , and reddening  $E(B - V)$ . Since the spectral index  $\alpha_\lambda$  and reddening  $E(B - V)$  are degenerate, the  $E(B - V)$  value derived from the fitting is not necessarily attached to any physical significance. Thus, the continuum is not corrected for any intrinsic reddening. To identify C IV BAL features, we smoothed the SDSS or BOSS spectrum using a 3 pixel boxcar and computed the AI parameter. For a quasar that has both SDSS and BOSS spectra, we consider it a BAL quasar if either of its spectra has AI > 0. Using this criterion, 173 additional BAL quasars were excluded, leaving us with 1957 quasars in the parent sample.

## 2.3. Measuring $f_{2500 \text{ \AA}}$

The measurement of the flux density at rest-frame 2500 Å ( $f_{2500 \text{ \AA}}$ ) is key for our analyses. In this paper, we derived the  $f_{2500 \text{ \AA}}$  values from the 2500 Å luminosities, which were converted from the absolute  $i$ -band magnitudes  $M_i(z = 2)$  using Equation 4 of Richards et al. (2006). The  $M_i(z = 2)$  values were adopted from the Shen et al. (2011) DR7 and Pâris et al. (2014) DR10 quasar catalogs. Since the absolute flux calibration errors in the BOSS spectra are relatively large and wavelength dependent (e.g., Pâris et al. 2012; Margala et al. 2016), we chose to estimate the  $f_{2500 \text{ \AA}}$  values from  $M_i(z = 2)$  instead of from spectral fitting for both SDSS DR7 and BOSS DR10 quasars to ensure homogeneous flux measurements.

We compared our  $f_{2500 \text{ \AA}}$  values for the DR7 quasars in our final sample (see Section 2.5 below) to those reported in the Shen et al. (2011) catalog. The Shen et al. (2011)  $f_{2500 \text{ \AA, Shen}}$  values, which were measured from spectral fitting, are largely consistent with our  $f_{2500 \text{ \AA}}$  values, with a mean  $f_{2500 \text{ \AA}}/f_{2500 \text{ \AA, Shen}}$  value of 0.99 and a standard deviation of 0.35. In addition, we verified that our  $f_{2500 \text{ \AA}}$  values are consistent with those ( $f_{2500 \text{ \AA, spec}}$ ) derived from our continuum fitting results in Section 2.2 (i.e., using power-law normalization, spectral index  $\alpha_\lambda$ , and reddening  $E(B - V)$ ) for the DR7 quasars in our final sample, with a mean  $f_{2500 \text{ \AA}}/f_{2500 \text{ \AA, spec}}$  value of 0.98 and a standard deviation of 0.28. We note that since the photometry and spectra are taken at different times, some of the standard deviation may just be due to quasar variability (rather than our methodological errors). For the DR10 quasars in our final sample (having BOSS spectra), we identified small wavelength dependent calibration offsets between the photometric magnitudes and the spectrum synthesized magnitudes (e.g., Margala et al. 2016), indicating

<sup>2</sup> See <http://cxc.cfa.harvard.edu/ciao/> for details.

<sup>3</sup> If a source has multiple *Chandra* observations, we selected the observation with the longest exposure and the smallest off-axis angle. Sources that lie within 32 pixels of any chip edge were excluded.

<sup>4</sup> There are 610 *Chandra* pointings that have two or more quasars within the field.

that any flux density measurements from the continuum fitting results in Section 2.2 may be unreliable.<sup>5</sup>

#### 2.4. Excluding RL Quasars

We also need to exclude radio-loud (RL) quasars, since they are well known to have X-ray emission levels systematically higher than those of radio-quiet (RQ) quasars with comparable optical/UV luminosities (e.g., Zamorani et al. 1981; Worrall et al. 1987). X-ray emission related to the jet, in addition to enhanced emission from the accretion-disk corona, may be required to interpret the X-ray excess of RL quasars (Miller et al. 2011; Zhu et al. 2020). Following Jiang et al. (2007), we matched the remaining sample of 1957 quasars to the latest Faint Images of the Radio Sky at Twenty-cm (FIRST; Becker et al. 1995) survey catalog (14Dec17 version)<sup>6</sup> with a matching radius of 30". We classified objects that have only one radio component within 5" as core-dominated quasars, and objects that have multiple radio components within 30" as lobe-dominated quasars. The sample contains 99 FIRST-detected quasars, including 80 core-dominated quasars and 19 lobe-dominated quasars. For each FIRST-detected object, we used the integrated flux density listed in the FIRST catalog to calculate its 1.4 GHz flux. For each lobe-dominated quasar, the total radio flux was calculated using all of its radio components within 30". We visually examined the quasar optical image from the Digital Sky Survey (DSS) to ensure that its radio components are not associated with any interloper. We also matched the 50 quasars that lie outside the FIRST survey area to the NRAO VLA Sky Survey (NVSS; Condon et al. 1998). Three objects have one NVSS source matched within 30". The upper limits on the 1.4 GHz fluxes for FIRST-undetected objects were set to  $0.25 + 3\sigma_{\text{rms}}$  mJy, where 0.25 is the CLEAN bias correction and  $\sigma_{\text{rms}}$  is the median rms noise of the FIRST survey (0.14; White et al. 1997); the upper limits on the 1.4 GHz fluxes for NVSS-undetected objects were set to 1.35 mJy, corresponding to three times the typical rms noise of the NVSS.

The radio-loudness parameter is defined as  $R = f_{5 \text{ GHz}}/f_{2500 \text{ \AA}}$  (e.g., Stocke et al. 1992), where  $f_{5 \text{ GHz}}$  is the flux density at rest-frame 5 GHz. The  $f_{5 \text{ GHz}}$  values (or their upper limits) were converted from the observed 1.4 GHz flux densities assuming a radio power-law slope of  $\alpha_r = -0.5$ . The FIRST survey is not sufficiently sensitive to discriminate  $R \geq 10$  vs.  $R < 10$  for a large fraction of our sample objects, and we therefore classify objects with  $R \geq 100$  as RL, objects

with  $10 \leq R < 100$  as radio-intermediate (RI), and objects with  $R < 10$  as RQ. There are 413 RQ, 30 RI, and 59 RL quasars within the remaining sample. Another 1455 objects with upper limits on  $R$  larger than 10 are referred to as radio-unclassified (RU), 97 of which have upper limits on  $R$  larger than 100. We excluded the 59 RL quasars, leaving 1898 objects in our sample.

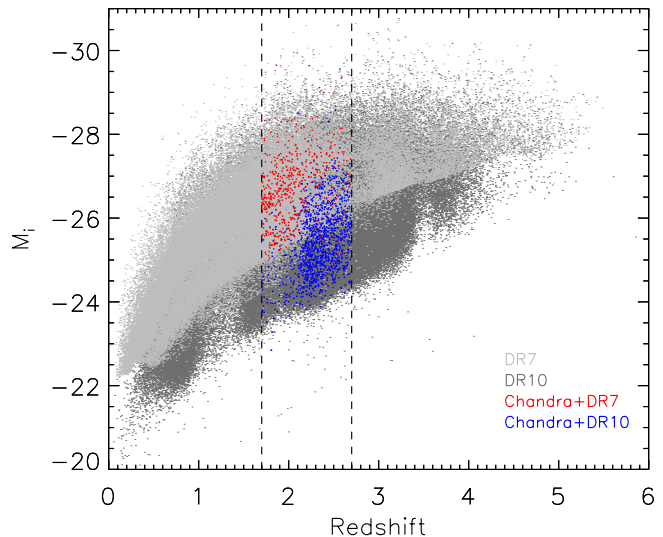


**Figure 1.** Redshift vs. absolute  $i$ -band magnitude for the 1825 quasars in the final sample (sample A); the red (blue) dots represent sample objects in the SDSS DR7 (DR10) catalog. The vertical dashed lines mark the redshift boundaries of  $z = 1.700$  and  $z = 2.700$ . The underlying light and dark gray dots represent all the SDSS DR7 and DR10 quasars, respectively.

#### 2.5. Final Sample

After excluding the BAL and RL quasars from the parent sample, we also removed 73 quasars that are *Chandra* targets; these X-ray targets might have unusual X-ray properties and they may bias our systematic investigation of X-ray weak quasars. The final sample contains 1825 quasars, and we refer to this sample as sample A. A summary of the sample selection is presented in Table 1. Sample A contains 555 DR7 quasars and 1270 DR10 quasars,<sup>7</sup> and we show in Figure 1 the 1825 sample A objects together with all the SDSS DR7 and DR10 quasars in the redshift versus absolute  $i$ -band magnitude  $M_i(z = 2)$  plane.

The X-ray observations for the sample A quasars are listed in Table 2. The measured  $f_{2500 \text{ \AA}}$  and  $R$  values (or

<sup>5</sup> We note that such small calibration errors hardly affect the computations of the AI parameters in Section 2.2 or the BI parameters in Pâris et al. (2014), and thus we do not consider the BAL quasar exclusion unreliable.

<sup>6</sup> <http://sundog.stsci.edu/>.

<sup>7</sup> There are 137 quasars in sample A that are in both the DR7 and DR10 quasar catalogs. We refer to these quasars as DR7 quasars, and we preferentially adopt their properties from the DR7 catalog.



**Table 1.** Sample Selection

Sample	Selection Criteria	Number of Quasars
Parent Sample	in DR7 or DR10 quasar catalog $1.700 < z < 2.700$	2475
	in <i>Chandra</i> Archive (07/01/2016)	
Sample A	in Parent Sample	1825
	excluding 518 BAL quasars	
	excluding 59 RL quasars excluding 73 <i>Chandra</i> targets	
Sample B	in Sample A	218
	in DR7 quasar catalog $m_i < 19.6$	
	effective exposure time $> 2.5$ ks off-axis angle $< 9.8'$	
Sample C	in Sample A	208
	in DR10 quasar catalog $m_i < 21.1$	
	effective exposure time $> 6.3$ ks off-axis angle $< 8.2'$	

their upper limits; see Section 2.4), along with the absolute  $i$ -band magnitudes  $M_i$ , REWs of the C IV  $\lambda 1549$  emission, and relative  $g - i$  colors (i.e.,  $\Delta(g - i)$ ; e.g., Richards et al. 2003) derived from the SDSS DR7 and DR10 quasar catalogs for the sample A objects are listed in Table 3. Properties from the SDSS DR7 quasar catalog are preferred when a quasar has an entry in both catalogs. We listed the C IV REW and  $\Delta(g - i)$  values, since weak C IV emission lines and red  $\Delta(g - i)$  colors are probably related to quasar X-ray weakness (see Sections 5.2.1 and 5.2.2 for further discussion). There are 31 DR10 quasars in sample A that have C IV  $\lambda 1549$  REW values of  $-1$  in the catalog, indicating that a principal component analysis (PCA) failed to fit the emission line (Pâris et al. 2014). For each of these objects, we fitted a power-law local continuum between rest-frame 1450–1470 and 1650–1820 Å, and then measured the C IV REW between 1500 and 1600 Å (see Section 7.3 of Pâris et al. 2012). The C IV REW values of these 31 DR10 quasars range from 0.9 to 479.1 Å, with a median value of 33.8 Å and a mean value of 84.5 Å.<sup>8</sup>

### 3. X-RAY DATA ANALYSIS

The X-ray data reduction was performed using CIAO version 4.8 and CALDB version 4.7.0. For each observation ID, we reprocessed the *Chandra* dataset using the CHANDRA\_REPRO script. Background flares were removed using the DEFLARE script with an iterative  $3\sigma$  clipping method.

<sup>8</sup> Adopting the same method, our measurements of the C IV REWs for other DR10 quasars in sample A are generally consistent with the C IV REWs reported in the Pâris et al. (2014) DR10 quasar catalog.

We made for each of the 1825 sample objects X-ray images in the 0.5–7 keV (broad), 0.5–2 keV (soft), and 2–7 keV (hard) bands from the cleaned level 2 event file. X-ray source detection was performed on the images using the WAVDETECT (Freeman et al. 2002) script with wavelet scales of 1, 1.414, 2, 2.828, 4, 5.656, and 8 pixels, and a significance threshold of  $10^{-6}$ . If a sample object is detected by WAVDETECT within  $3.0''$  of the SDSS position, we used the WAVDETECT position as its X-ray position; otherwise, we used the SDSS astrometry as the X-ray position. Aperture photometry was performed to extract source counts in the broad, soft, and hard bands. We used circular and annular regions centered at the X-ray position to extract source and background counts, respectively. The radius of the circle was chosen to enclose 90% of the point spread function (PSF) at 1 keV, while the inner and outer radii of the annulus were chosen to be the source radius plus 15 and 50 pixels, respectively. We visually inspected the background-extraction region for each sample object. In cases where any WAVDETECT source contaminates the background region, we excluded its elliptical WAVDETECT region that contains the majority of the source counts from the annulus. We manually changed the annulus to a pie-shaped region<sup>9</sup> whenever the background region is partially off-chip.

To assess the detection significance, we calculated in each of the broad, soft, and hard bands a binomial no-source probability  $P_B$  using the following equation (e.g., Xue et al. 2011; Luo et al. 2013, 2015):

$$P_B(X \geq S) = \sum_{X=S}^N \frac{N!}{X!(N-X)!} p^X (1-p)^{N-X}, \quad (2)$$

where  $S$  is the total counts in the source-extraction region;  $N = S + B$ , where  $B$  is the total counts in the background-extraction region;  $p = 1/(1 + BACKSCAL)$ , where  $BACKSCAL$  is the background-to-source area ratio. If a sample object satisfied  $P_B < 0.01$  in one band, we consider it detected in this band and calculated net counts along with associated  $1\sigma$  errors, derived from  $1\sigma$  errors (Gehrels 1986) on the source and background counts; otherwise we consider it undetected in this band and calculated a  $3\sigma$  confidence level upper limit on the source counts using the Bayesian method of Kraft et al. (1991). We consider a source X-ray detected if it is detected in one or more of the three X-ray bands. Our sample A contains 1344 X-ray detected and 481 X-ray undetected quasars. Figure 2 shows the distributions of the broad-band effective exposure times and off-axis angles for these X-ray detected and X-ray undetected objects. The effective exposure time is the exposure time that has been corrected for the effects of

<sup>9</sup> See <https://cxc.cfa.harvard.edu/ciao/ahelp/dmregions.html> for a description of the pie-shaped region.

**Table 2.** *Chandra* Observations and X-ray Photometric Properties

SDSS Name	Data Release	Redshift	Observation	Exposure	Broad Band	Soft Band	Hard Band	Band	$\Gamma_{\text{eff}}$	Sample B	Sample C
(J2000)			ID	Time (ks)	(0.5–7 keV)	(0.5–2 keV)	(2–7 keV)	Ratio			
(1)	(2)	(3)	(4)	(5)	(6)	(7)	(8)	(9)	(10)	(11)	(12)
000015.47 + 005246.8	7	1.8571	11591	21.7	$61.5^{+9.7}_{-8.6}$	$40.1^{+7.7}_{-6.6}$	$21.4^{+6.6}_{-5.5}$	$0.53^{+0.18}_{-0.15}$	$1.6^{+0.3}_{-0.3}$	0	0
000018.18 + 050803.6	10	2.2279	7334	2.7	< 8.3	< 8.7	< 5.9	...	1.8	0	0
000029.98 + 004845.3	10	2.4120	11591	21.2	$11.3^{+6.3}_{-5.2}$	$6.8^{+4.5}_{-3.4}$	< 18.6	$0.79^{+1.48}_{-0.60}$	$1.1^{+1.4}_{-1.0}$	0	0
000106.87 + 023845.9	10	1.7600	4837	5.0	$4.5^{+3.4}_{-2.2}$	$4.7^{+3.4}_{-2.2}$	< 5.9	$0.15^{+0.22}_{-0.14}$	$2.6^{+2.0}_{-0.9}$	0	0
000159.88 + 003715.5	10	2.3910	4861	4.8	< 16.7	< 13.2	< 11.3	...	1.8	0	0

NOTE— Cols. (1)–(3): SDSS name in the J2000 equatorial coordinate format, SDSS Data Release number, and redshift. The improved redshifts from [Hewett & Wild \(2010\)](#) reported in the [Shen et al. \(2011\)](#) catalog are listed for the DR7 quasars. Col. (4): *Chandra* observation ID. Col. (5): *Chandra* effective exposure time in the broad (0.5–7 keV) band. Cols. (6)–(8): broad-band (0.5–7 keV), soft-band (0.5–2 keV), and hard-band (2–7 keV) net counts in the source region. A  $3\sigma$  confidence level upper limit on the source counts is given if the source is undetected. Col. (9): band ratio between the hard-band and soft-band counts. An entry of “...” indicates that the source is undetected in both bands. Col. (10): 0.5–7 keV effective power-law photon index derived from the band ratio. It is fixed at 1.8 for any source that is undetected in both the soft and hard bands (see Section 3). Cols. (11) and (12): an entry of “1” indicates that the object is in sample B or sample C (see Section 4.3). Table 2 is sorted by increasing J2000 right ascension and is published in its entirety in the electronic edition of the journal. A portion is shown here for guidance regarding its form and content.

**Table 3.** X-ray and Optical Properties

SDSS Name	$M_i$	$f_{2 \text{ keV}}$	$F_{0.5-7 \text{ keV}}$	$\log L_{2-10 \text{ keV}}$	$f_{2500 \text{ \AA}}$	$\alpha_{\text{OX}}$	$\Delta\alpha_{\text{OX}}$	$f_{\text{weak}}$	REW C IV	$\Delta(g-i)$	$R$	X-ray Weak
(1)	(2)	(3)	(4)	(5)	(6)	(7)	(8)	(9)	(10)	(11)	(12)	(13)
000015.47 + 005246.8	-26.19	6.36	4.26	44.75	0.52	-1.50	0.00	1.0	44.1	0.131	< 12.0	0
000018.18 + 050803.6	-25.75	< 10.85	< 5.40	< 45.06	0.25	< -1.29	< 0.17	> 0.4	57.0	0.056	< 26.5	0
000029.98 + 004845.3	-24.43	0.74	0.91	44.22	0.06	-1.51	-0.17	2.7	78.9	0.047	< 106.0	0
000106.87 + 023845.9	-23.98	2.92	0.82	44.03	0.07	-1.31	-0.00	1.0	51.6	-0.085	< 82.5	0
000159.88 + 003715.5	-24.88	< 9.55	< 4.57	< 45.06	0.10	< -1.16	< 0.23	> 0.3	43.4	-0.031	< 68.9	0

NOTE— Cols. (1) and (2): SDSS name in the J2000 equatorial coordinate format and absolute  $i$ -band magnitude. Col. (3): rest-frame 2 keV flux density in units of  $10^{-32} \text{ erg cm}^{-2} \text{ s}^{-1} \text{ Hz}^{-1}$ . A  $3\sigma$  confidence level upper limit on  $f_{2 \text{ keV}}$  is given if the source is undetected. Cols. (4) and (5): observed-frame 0.5–7 keV flux in units of  $10^{-14} \text{ erg cm}^{-2} \text{ s}^{-1}$  and logarithm of the rest-frame 2–10 keV luminosity in units of  $\text{erg s}^{-1}$ , both calculated using  $f_{2 \text{ keV}}$  and  $\Gamma_{\text{eff}}$  (see Table 2). Col. (6): rest-frame 2500 Å flux density in units of  $10^{-27} \text{ erg cm}^{-2} \text{ s}^{-1} \text{ Hz}^{-1}$ . Col. (7): measured X-ray-to-optical power-law slope  $\alpha_{\text{OX}}$ . A  $3\sigma$  confidence level upper limit on  $\alpha_{\text{OX}}$  is given if the source is undetected. Col. (8): difference between the measured  $\alpha_{\text{OX}}$  and that expected from our best-fit  $\alpha_{\text{OX}}-L_{2500 \text{ \AA}}$  relation. Col. (9): X-ray weakness factor measured from  $\Delta\alpha_{\text{OX}}$ . Col. (10): REW (in units of Å) of the C IV  $\lambda 1549$  emission line. Col. (11): relative  $g-i$  color. Col. (12): radio-loudness parameter. Col. (13): an entry of “1” indicates that the object is X-ray weak. We adopted  $\Delta\alpha_{\text{OX}} = -0.3$  to be the threshold separating X-ray normal and X-ray weak quasars (see Section 4.2). Table 3 is sorted by increasing J2000 right ascension and is published in its entirety in the electronic edition of the journal. A portion is shown here for guidance regarding its form and content.

vignetting and CCD gaps. The X-ray detected quasars in general have longer exposures and smaller off-axis angles than the X-ray undetected quasars. The numbers of detected/undetected DR7/DR10 quasars in specific X-ray bands are listed in Table 4.

Assuming power-law X-ray spectra modified by Galactic absorption, we derived the effective power-law photon indices ( $\Gamma_{\text{eff}}$ ) from the band ratios for the 1285 sample objects that are detected in at least one of the soft and hard bands. The band ratio is defined as the ratio between the hard-band and soft-band counts. For each of the 732 objects that are detected in both the soft and hard bands, the band ratio was calculated by dividing the hard-band net counts by the soft-band net counts, and its associated  $1\sigma$  uncertainties were derived using the method of Bayesian estimation of hardness ratios (BEHR; [Park et al. 2006](#)). For each of the 553 objects

that are detected in only one of the soft and hard bands, we adopted the band ratio to be the mode of its posterior probability distribution computed using BEHR ([Park et al. 2006](#)). These are best-guess estimates, and they appear more appropriate for deriving source fluxes than assuming a fixed spectral shape ([Luo et al. 2017](#)). To derive  $\Gamma_{\text{eff}}$  from the band ratio, we used the CIAO SPECEXTRACT script to create the source spectrum, auxiliary response file (ARF), and redistribution matrix file (RMF). We then used the Sherpa (CIAO’s modeling and fitting package; e.g., [Freeman et al. 2001](#)) FAKE\_PHA command to create simulated spectra for a power-law plus Galactic absorption model with varying  $\Gamma$ . The observed band ratio was compared to the modeled band ratios, and the value of  $\Gamma_{\text{eff}}$  was determined by interpolating the modeled  $\Gamma$  values.

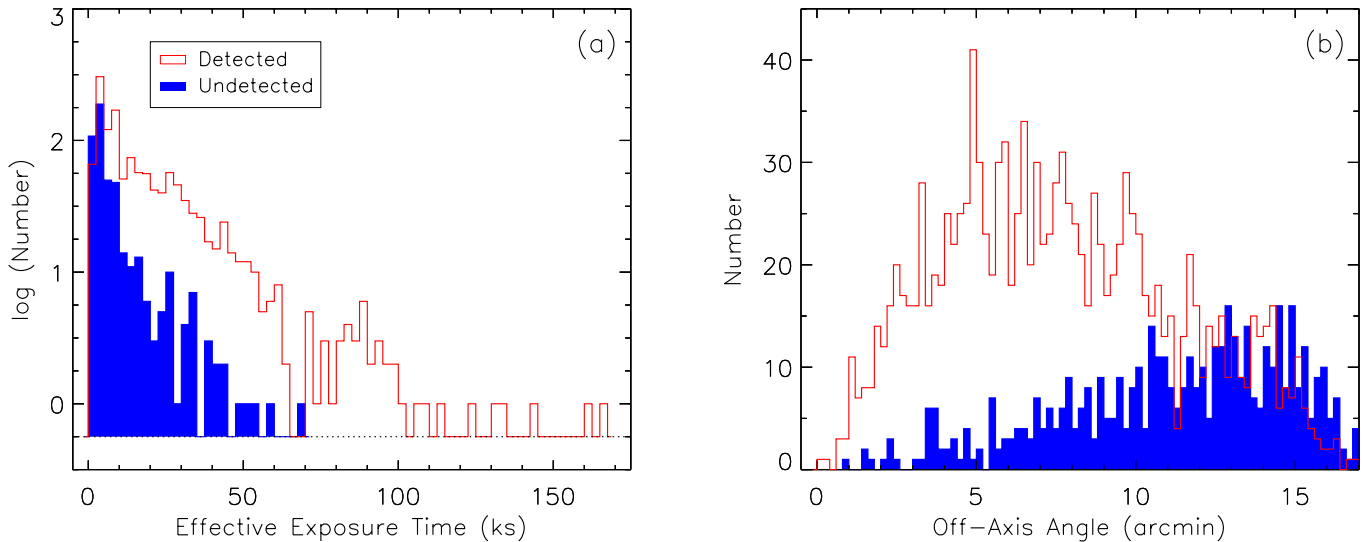


**Figure 2.** Distributions of the (a) effective exposure time in the broad band (0.5–7 keV) and (b) off-axis angle for sample A. The open red and solid blue histograms represent the X-ray detected and X-ray undetected objects, respectively. In the left panel, the  $y$ -axis is logarithmic, bins with zero counts are set to  $-0.25$  (dotted horizontal line). In the right panel, there is one sample object that has a small off-axis angle of  $8.4''$ . We note that it is not the target of the corresponding *Chandra* observation.

For each of the 540 quasars that are undetected in both the soft and hard bands (including 59 objects detected only in the broad band), the band ratio is not available; thus we adopted a fixed  $\Gamma_{\text{eff}}$  value of 1.8, which is around the median value of  $\Gamma_{\text{eff}}$  for sample A objects (see Section 4.1 below). Among the 540 quasars with fixed  $\Gamma_{\text{eff}}$  values, there are three X-ray detected (i.e., detected only in the broad band) objects having  $\Delta\alpha_{\text{OX}} \leq -0.3$  and one X-ray undetected object having an upper limit on  $\Delta\alpha_{\text{OX}} \leq -0.3$ ; these four objects are considered X-ray weak (see Section 4.2 below). Since the detected X-ray weak quasars have a median  $\Gamma_{\text{eff}}$  value of 0.8 (see Section 4.2 below), these four quasars likely have smaller  $\Gamma_{\text{eff}}$  values. However, as their number is small and they may also be intrinsically X-ray weak quasar candidates, we still chose to adopt  $\Gamma_{\text{eff}} = 1.8$  to calculate the relevant parameters (or their upper limits); adopting smaller  $\Gamma_{\text{eff}}$  values (e.g., 0.8) for these four quasars would not affect significantly our results. The X-ray properties for sample A are listed in Table 2.

## 4. RESULTS

### 4.1. $\alpha_{\text{OX}}-L_{2500 \text{ \AA}}$ Relation

The X-ray-to-optical power-law slope parameter  $\alpha_{\text{OX}}$  or its upper limit was measured for each of our sample objects. For each of the 1344 X-ray detected objects, we derived its rest-frame 2 keV flux density ( $f_{2 \text{ keV}}$ ) by normalizing the broad-band counts in the simulated spectrum with the derived  $\Gamma_{\text{eff}}$  value (see Section 3) to the observed broad-band net counts. If a sample object is undetected in the broad band but detected in the soft (or hard) band, we normalized the soft-band (or hard-

band) counts in the simulated spectrum to the observed net counts. For each of the 481 X-ray undetected objects, a  $3\sigma$  confidence level upper limit on  $f_{2 \text{ keV}}$  was computed by normalizing the broad-band counts in the simulated spectrum to the upper limit on the observed broad-band counts (Section 3). The  $3\sigma$  upper limit is appropriate for the following survival analysis. The  $f_{2 \text{ keV}}$  and  $\alpha_{\text{OX}}$  parameters are listed in Table 3.

Previous studies have revealed a strong anticorrelation between  $\alpha_{\text{OX}}$  and 2500 Å monochromatic luminosity over five orders of magnitude in  $L_{2500 \text{ \AA}}$  (e.g., Wilkes et al. 1994; Strateva et al. 2005; Steffen et al. 2006; Just et al. 2007). Figure 3 shows the  $\alpha_{\text{OX}}$  versus  $L_{2500 \text{ \AA}}$  distribution for our sample A quasars. The generalized Kendall’s  $\tau$  test in the Astronomy Survival Analysis package (ASURV Rev 1.2; Isobe & Feigelson 1990; LaValley et al. 1992) confirmed a highly significant ( $20.4\sigma$ ) anticorrelation between  $\alpha_{\text{OX}}$  and  $L_{2500 \text{ \AA}}$ .

Before quantifying the  $\alpha_{\text{OX}}-L_{2500 \text{ \AA}}$  relation, we attempted to exclude potentially X-ray absorbed objects. We selected potentially X-ray absorbed objects based on the effective power-law photon index  $\Gamma_{\text{eff}}$ . The mean value of  $\Gamma_{\text{eff}}$  for RQ type 1 quasars has been found to be  $\Gamma \approx 1.9$  (e.g., Reeves et al. 1997; Just et al. 2007). The  $\Gamma_{\text{eff}}$  value generally becomes smaller if a quasar is X-ray absorbed. For the 1285 quasars in our sample that are detected in at least one of the soft and hard bands, the distribution of  $\Gamma_{\text{eff}}$  is shown Figure 4(a). The  $\Gamma_{\text{eff}}$  values range from  $-1.4$  to  $4.0$  with an average value of 1.8 and a standard deviation of 0.7, consistent with those derived in previous studies (e.g., Just et al. 2007).

**Table 4.** Numbers of X-ray Detected/Undetected DR7/DR10 Quasars in Samples A, B, and C

X-ray Detection Breakdown	Sample A			Sample B	Sample C
	DR7	DR10	All	DR7	DR10
Detected in the Broad Band	473	806	1279	216	207
Detected in the Soft Band	475	781	1256	214	198
Detected in the Hard Band	321	440	761	179	158
Detected in <i>Both</i> the Soft and Hard Bands	317	415	732	177	155
Detected in <i>Only One</i> of the Soft and Hard Bands	162	391	553	39	46
X-ray Detected	490	854	1344	218	208
X-ray Undetected	65	416	481	0	0

NOTE—We consider a source X-ray detected if it is detected in at least one of the three X-ray bands and consider a source X-ray undetected if it is undetected in all three X-ray bands. All objects in samples B and C are X-ray detected.

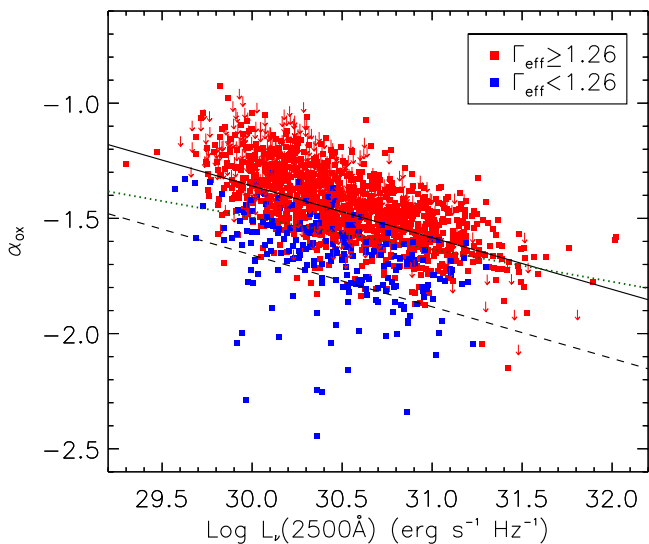


**Figure 3.**  $\alpha_{\text{OX}}$  vs. 2500 Å monochromatic luminosity for sample A. The red and blue filled squares represent X-ray unabsorbed ( $\Gamma \geq 1.26$ ) and potentially X-ray absorbed objects ( $\Gamma < 1.26$ ), respectively; downward arrows represent the  $3\sigma$  upper limits on  $\alpha_{\text{OX}}$ . The solid black line shows the best-fit relation for the 1595  $\Gamma \geq 1.26$  objects, while the dashed black line shows  $\Delta\alpha_{\text{OX}} = -0.3$  from the best-fit relation, separating X-ray normal and X-ray weak quasars (see Section 4.2 below). The green dotted line shows the [Just et al. \(2007\)](#)  $\alpha_{\text{OX}}-L_{2500 \text{ Å}}$  relation for comparison.

We fitted the  $\Gamma_{\text{eff}}$  distribution with a Gaussian function using the IDL MPFIT ([Markwardt 2009](#)) routine. The black curve in Figure 4(a) is the best-fit Gaussian profile, which has a mean of 1.78 and a standard deviation of 0.52. We note that there are 553 objects among these 1285 quasars that are detected in only one

of the soft and hard bands, and their  $\Gamma_{\text{eff}}$  values are best-guess estimates (Section 3). The  $\Gamma_{\text{eff}}$  values that deviate from the mean by more than  $2.5\sigma$  (i.e.,  $\Gamma_{\text{eff}} \lesssim 0.5$  or  $\Gamma_{\text{eff}} \gtrsim 3.1$ ) come predominantly from these 553 objects. Excluding these 553 objects, the distribution of  $\Gamma_{\text{eff}}$  for the 732 objects that are detected in both the soft and hard bands is shown in Figure 4(b). The best-fit Gaussian profile has a mean of 1.70 and a standard deviation of 0.45.

Based on the above  $\Gamma_{\text{eff}}$  distributions, we adopted  $\Gamma = 1.26$  to be the threshold separating X-ray unabsorbed and potentially X-ray absorbed quasars in this paper (i.e., an object with  $\Gamma_{\text{eff}} < 1.26$  is considered an absorbed quasar), which corresponds to a negative  $1\sigma$  deviation from the means of the Gaussian distributions. We have verified that adopting a larger  $\Gamma_{\text{eff}}$  value of 1.4 as the threshold would not affect significantly our results below. We thus excluded 230 quasars with  $\Gamma < 1.26$  in our sample when fitting the  $\alpha_{\text{OX}}-L_{2500 \text{ Å}}$  relation. We utilized the EM (estimate and maximize) algorithm in ASURV to derive the linear regression parameters. The best-fit relation for the remaining 1595 quasars is

$$\alpha_{\text{OX}} = (-0.224 \pm 0.008) \log(L_{2500 \text{ Å}}) + (5.373 \pm 0.254), \quad (3)$$

which is shown as the solid black line in Figure 3. The [Just et al. \(2007\)](#)  $\alpha_{\text{OX}}-L_{2500 \text{ Å}}$  relation is shown for comparison.

The slope of the best-fit  $\alpha_{\text{OX}}-L_{2500 \text{ Å}}$  relation is steeper than that from [Just et al. \(2007\)](#). We note that our sample A spans about three orders of magnitude in  $L_{2500 \text{ Å}}$  [ $29.3 \lesssim \log(L_{2500 \text{ Å}}) \lesssim 32.0$ ], while the [Just et al. \(2007\)](#) sample spans a much larger  $L_{2500 \text{ Å}}$  range and extends to lower luminosities [ $27.5 \lesssim \log(L_{2500 \text{ Å}}) \lesssim 32.5$ ]. Therefore, the apparent difference between the  $\alpha_{\text{OX}}-L_{2500 \text{ Å}}$  slopes of this study



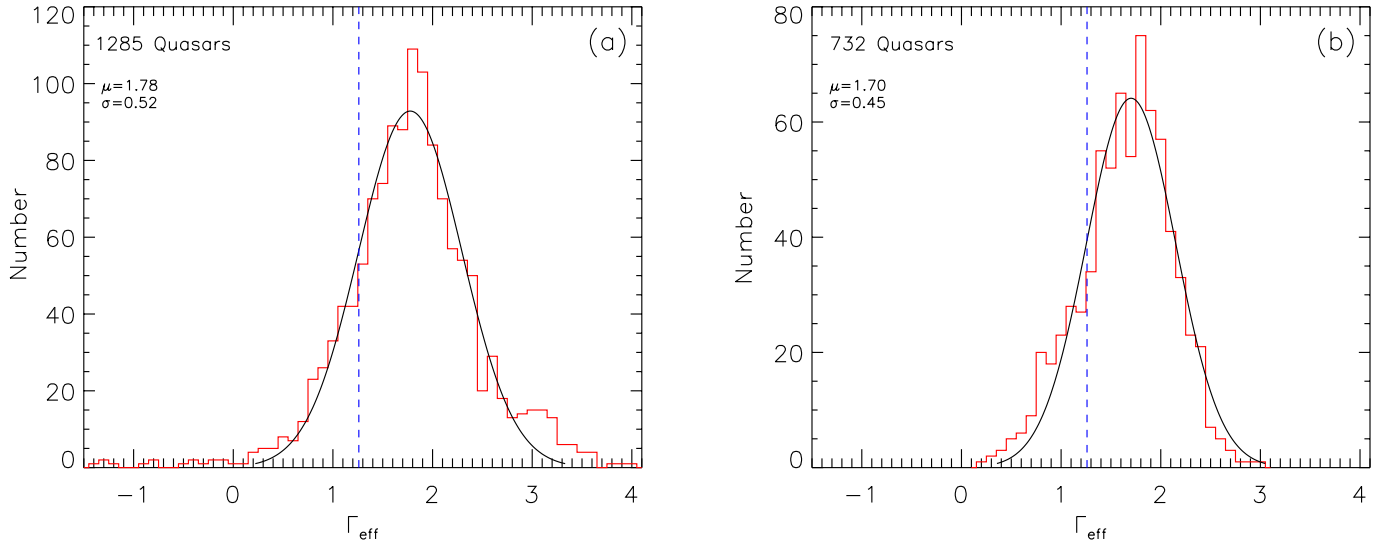


**Figure 4.** Distribution of  $\Gamma_{\text{eff}}$  for (a) 1285 quasars that are detected in at least one of the soft and hard bands, and (b) 732 quasars that are detected in both the soft and hard bands. In each panel, the black curve shows the best-fit Gaussian profile, with the mean and standard deviation of the Gaussian fit listed in the upper left corner; the vertical dashed line indicates  $\Gamma_{\text{eff}} = 1.26$ , which is the threshold adopted in this study to separate X-ray unabsorbed and potentially X-ray absorbed quasars.

and Just et al. (2007) may result from the different UV luminosity ranges. The difference is consistent with the Steffen et al. (2006) interpretation that the  $\alpha_{\text{OX}}-L_{2500 \text{ \AA}}$  slope becomes steeper at higher UV luminosities. We also note that our  $\alpha_{\text{OX}}-L_{2500 \text{ \AA}}$  relation is consistent with that derived in a recent study by Timlin et al. (2020).

#### 4.2. X-ray Weak Quasars and Their Fraction

We calculated the  $\Delta\alpha_{\text{OX}}$  parameter, defined as the difference between the measured  $\alpha_{\text{OX}}$  and that expected from the best-fit  $\alpha_{\text{OX}}-L_{2500 \text{ \AA}}$  relation (Equation 3),  $\Delta\alpha_{\text{OX}} = \alpha_{\text{OX}} - \alpha_{\text{OX}}(L_{2500 \text{ \AA}})$ . In order to define the X-ray weak population, we examined the distribution of  $\Delta\alpha_{\text{OX}}$  values, which is shown in Figure 5. Of the 1825 objects in our sample, 65 (including one X-ray undetected object) have  $\Delta\alpha_{\text{OX}} \leq -0.3$  but only 11 have  $\Delta\alpha_{\text{OX}} \geq 0.3$ , which causes the apparent asymmetry of the  $\Delta\alpha_{\text{OX}}$  distribution. The distribution of the X-ray detected objects can be well described by a Gaussian profile plus a negative tail with  $\Delta\alpha_{\text{OX}} < -0.3$ , indicating the existence of a small population of X-ray weak quasars. Based on the  $\Delta\alpha_{\text{OX}}$  distribution, we adopted  $\Delta\alpha_{\text{OX}} = -0.3$  as the threshold separating X-ray normal and X-ray weak quasars in this paper (i.e., an object with  $\Delta\alpha_{\text{OX}} \leq -0.3$  is considered an X-ray weak quasar). We note that the  $\Delta\alpha_{\text{OX}}$  distribution for the 1114  $\Gamma \geq 1.26$  X-ray detected objects (Section 4.1) has a standard deviation of 0.12. Thus,  $\Delta\alpha_{\text{OX}} = -0.3$  corresponds to a negative  $2.5\sigma$  deviation from the zero point.

Gibson et al. (2008a) have measured upper limits on the fractions of quasars that are X-ray weak by given factors. In this study, as the number of X-ray quasars has been increased significantly, we can better constrain the X-ray weak fractions. Considering that the X-ray undetected quasars have only upper limit constraints on their X-ray weakness factors, we utilized the Kaplan-Meier estimator provided in the ASURV package, which works with censored data, to derive the best estimates and uncertainties for these fractions. Figure 6 shows the fraction of quasars with  $f_{\text{weak}} \geq x$  versus  $x$ . The X-ray weakness factor  $f_{\text{weak}}$  was measured from  $\Delta\alpha_{\text{OX}}$  as  $f_{\text{weak}} = 10^{-\Delta\alpha_{\text{OX}}/0.3838}$ , and the X-ray weak threshold  $\Delta\alpha_{\text{OX}} \leq -0.3$  corresponds to an X-ray weakness factor of  $f_{\text{weak}} \geq 6.0$ . We found the fraction of X-ray weak quasars to be  $5.8 \pm 0.7\%$ ; the  $1\sigma$  uncertainties were calculated following the method of Avni et al. (1980). Additionally, the fractions of quasars that are X-ray weak by factors of  $f_{\text{weak}} \geq 10$  ( $\Delta\alpha_{\text{OX}} \leq -0.38$ ),  $f_{\text{weak}} \geq 20$  ( $\Delta\alpha_{\text{OX}} \leq -0.50$ ), and  $f_{\text{weak}} \geq 50$  ( $\Delta\alpha_{\text{OX}} \leq -0.65$ ) are  $2.7 \pm 0.5\%$ ,  $1.3 \pm 0.3\%$ , and  $0.74 \pm 0.26\%$ , respectively.

#### 4.3. Fractions of X-ray Weak Quasars among Two Subsamples

We note that the Kaplan-Meier estimator used in Section 4.2 assumes that the intrinsic distribution of the censored data is the same as that of the measured data (Feigelson & Nelson 1985). The assumption is sensible if the X-ray nondetections are simply caused by shallower Chandra coverage, but it is not valid if many of the X-ray undetected quasars are indeed more X-ray weak (having a more negative  $\Delta\alpha_{\text{OX}}$  distribution) than the

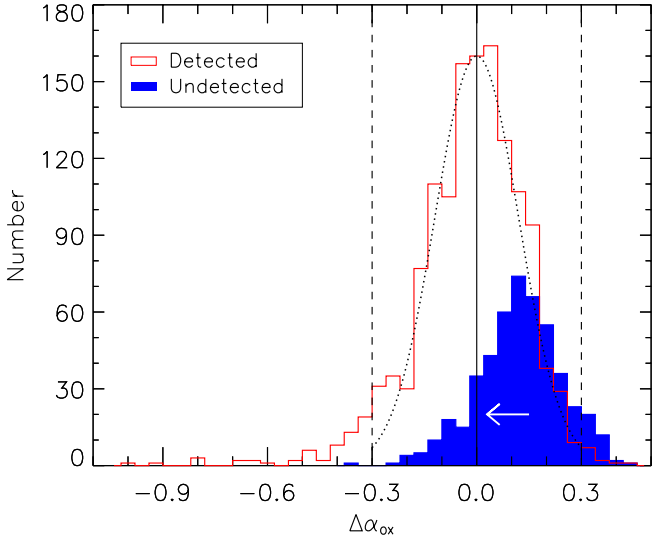


**Figure 5.** Distributions of the  $\Delta\alpha_{\text{OX}}$  values for sample A. The open red histogram represents the distribution for the X-ray detected objects, while the solid blue histogram represents the distribution of the  $3\sigma$  upper limits on  $\Delta\alpha_{\text{OX}}$  for the X-ray undetected objects. The arrow indicates that the blue histogram is the distribution of upper limits. The vertical dashed lines (solid line) indicate  $\Delta\alpha_{\text{OX}} = \pm 0.3$  ( $\Delta\alpha_{\text{OX}} = 0$ ) from the best-fit  $\alpha_{\text{OX}}-L_{2500 \text{ \AA}}$  relation (Equation 3; see Section 4.1). The black dotted curve shows a Gaussian profile with a mean value of 0 and a standard deviation of 0.12; it is not a fit to the  $\Delta\alpha_{\text{OX}}$  distribution but is drawn to guide the eye.

X-ray detected quasars. Given Figure 2, it appears that the X-ray undetected quasars in general have shallower Chandra coverage than the X-ray detected quasars, but it is not sufficient to justify the assumption above, especially when we are interested in the exceptionally X-ray weak quasars. Therefore, in this subsection, we constructed, without direct reference to X-ray source properties, two subsamples of quasars out of sample A that do not have censored  $\Delta\alpha_{\text{OX}}$  values (all X-ray detected), and then we compared the fractions of X-ray weak quasars among these subsamples to that in sample A.

The principle to select quasars that are likely X-ray detected is to limit the sample to bright quasars and to also limit the X-ray observations to those with good sensitivity (relatively large exposures and small off-axis angles; e.g., Figure 2). Because the DR7 and DR10 quasar catalogs have significantly different depths, we cannot select bright quasars from these two catalogs using a uniform brightness criterion. Thus, we constructed a subsample of quasars from the DR7 and DR10 catalogs, respectively. The detailed criteria are as follows:

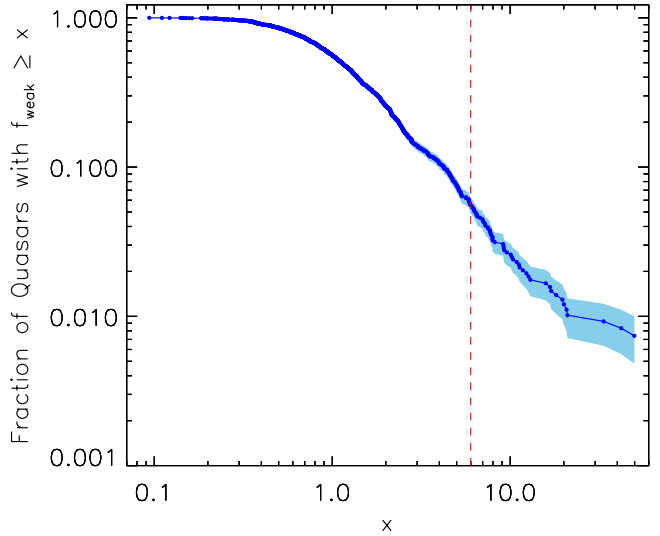


**Figure 6.** Fraction of quasars with  $f_{\text{weak}} \geq x$  vs.  $x$ . The shaded region indicates the  $1\sigma$  confidence intervals calculated following the method of Avni et al. (1980). The vertical line shows  $f_{\text{weak}} \geq 6$  ( $\Delta\alpha_{\text{OX}} \leq -0.3$ ), which is the threshold separating X-ray normal and X-ray weak quasars.

1.  $i$ -band magnitude  $m_i < 19.6$  ( $m_i < 21.1$ ) for DR7 (DR10) quasars,
2. effective exposure time  $> 2.5$  ks ( $> 6.3$  ks) and off-axis angle  $< 9.8'$  ( $< 8.2'$ ) for DR7 (DR10) quasars. We adopted more stringent exposure-time and off-axis angle criteria for DR10 quasars, since they are on average optically fainter than DR7 quasars.

These two criteria resulted in a subsample of 218 (208) quasars in DR7 (DR10), and we refer to this subsample as sample B (sample C). The selections of samples B and C are also listed in Table 1. Quasars in sample B or sample C are all X-ray detected, and thus we can compute the fraction of X-ray weak quasars among each subsample directly, without employing the Kaplan-Meier estimator. We stress that we do not require X-ray detections in the construction of samples B and C, which are simply the outcomes of the appropriate brightness and X-ray sensitivity criteria listed above.

Given our X-ray weak definition of  $\Delta\alpha_{\text{OX}} \leq -0.3$ , sample B contains 12 X-ray weak quasars, corresponding to an X-ray weak fraction of  $5.5^{+2.0}_{-1.2}\%$  (12/218); the  $1\sigma$  binomial confidence intervals were calculated following the method of Cameron (2011). Figure 7(a) shows the fraction of quasars with  $f_{\text{weak}} \geq x$  versus  $x$  in sample B. The fraction of quasars that are X-ray weak by a factor of  $f_{\text{weak}} \geq 10$  ( $\Delta\alpha_{\text{OX}} \leq -0.38$ ) in sample B is  $3.2^{+1.7}_{-0.8}\%$  (7/218). In sample C, there are 14 X-ray weak quasars, corresponding to an X-ray weak fraction of  $6.7^{+2.2}_{-1.4}\%$  (14/208). Figure 7(b) shows the fraction of quasars with  $f_{\text{weak}} \geq x$  versus  $x$  in sample C. The  $f_{\text{weak}} \geq 10$  frac-

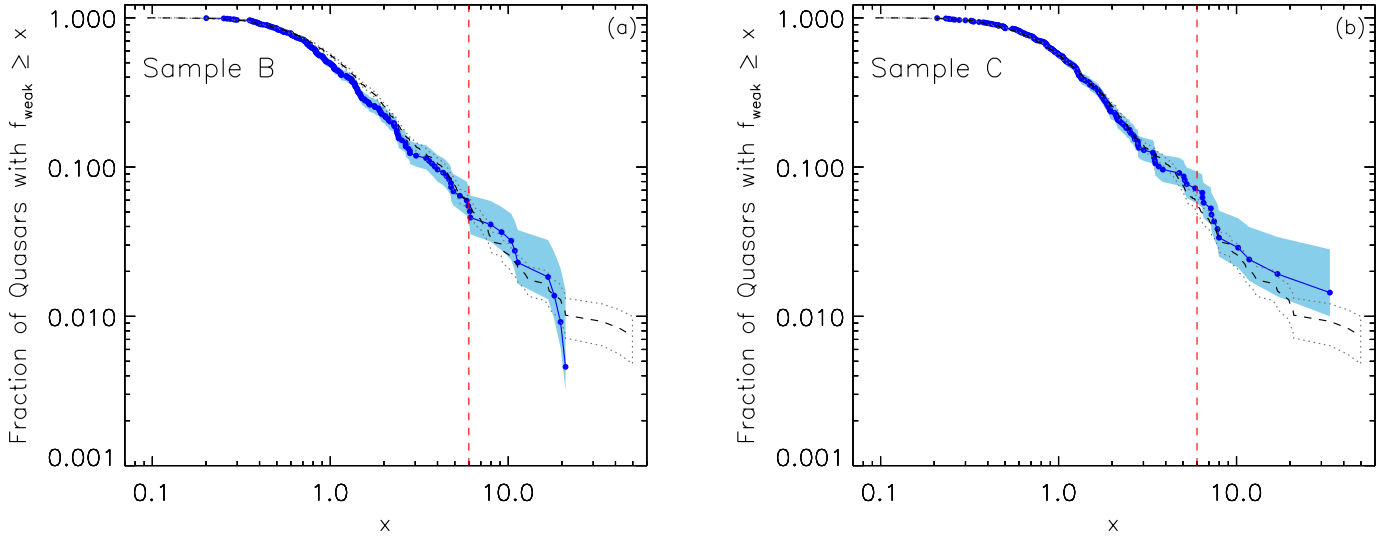


**Figure 7.** Fraction of quasars with  $f_{\text{weak}} \geq x$  vs.  $x$  for (a) sample B and (b) sample C. The shaded region indicates the  $1\sigma$  binomial confidence intervals calculated following the method of Cameron (2011). The vertical line in each panel shows  $f_{\text{weak}} \geq 6$  ( $\Delta\alpha_{\text{OX}} \leq -0.3$ ), which is the threshold separating X-ray normal and X-ray weak quasars. The X-ray weak fraction (black dashed curve) and associated  $1\sigma$  confidence intervals (black dotted curves) for sample A are plotted in both panels for comparison.

tion in sample C is  $2.9^{+1.7}_{-0.8}\%$  (6/208). The X-ray weak fraction curve for sample A is also plotted in Figure 7, showing general consistency with the curve for sample B or sample C.

We note that the fractions of X-ray weak quasars among samples B and C are consistent within the uncertainties. Samples B and C probe slightly different quasar populations in terms of their optical brightness and X-ray coverage, and the fractions of X-ray weak quasars among them are not necessarily the same, but our current data is not sufficient to determine if the fraction has any luminosity dependence. In order to increase the sample size and reduce the fraction uncertainties, we combine samples B and C (sample B+C) in our following analysis. In this combined sample, the X-ray weak and  $f_{\text{weak}} \geq 10$  fractions become  $6.1^{+1.4}_{-1.0}\%$  (26/426) and  $3.1^{+1.1}_{-0.6}\%$  (13/426), respectively. Comparing these fractions to those in sample A, we found that they are consistent within the uncertainties. The Kaplan-Meier estimator appears to provide a reasonable estimate of the fraction of X-ray weak quasars in sample A, and the difference between the quasar populations in sample A and sample B+C does not appear to affect significantly the X-ray weak fractions.

## 5. DISCUSSION

### 5.1. Fractions of X-ray Weak Quasars

Our study found that a small fraction of optically selected, non-BAL, type 1 quasars do show weak X-ray emission. Based on our sample A of 1825 quasars, 1344 ( $74 \pm 1\%$ ) of which are X-ray detected, the fraction of

X-ray weak ( $f_{\text{weak}} \geq 6$ ) quasars is  $5.8 \pm 0.7\%$  and the fraction of  $f_{\text{weak}} \geq 10$  quasars is  $2.7 \pm 0.5\%$ . Based on our subsample B+C of 426 quasars that are composed of X-ray detections only, the fraction of X-ray weak quasars is  $6.1^{+1.4}_{-1.0}\%$  and the fraction of  $f_{\text{weak}} \geq 10$  quasars is  $3.1^{+1.1}_{-0.6}\%$ . These small but non-negligible fractions of X-ray weak quasars challenge the ubiquity of quasar X-ray emission, and they also require additional physical mechanisms internal or external to the corona that can suppress the observed X-ray emission; we discuss some possible causes for the X-ray weak quasars in Section 5.2 below.

Our current investigation was motivated by the Gibson et al. (2008a) study that used a much smaller sample of quasars. Based on the sample B of Gibson et al. (2008a), which is similar to our sample B+C here composed of X-ray detections only but has only 139 quasars, the fraction of  $f_{\text{weak}} \geq 10$  quasars is considered to be  $\lesssim 2\%$ . Their result is consistent with ours here considering the uncertainties of both studies.

Recently, a few studies have found much larger fractions of X-ray weak quasars, albeit among samples with very limited sizes. For example, Nardini et al. (2019) found seven X-ray weak quasars among 29 very luminous RQ quasars at  $z \approx 3.0$ – $3.3$ , corresponding to an X-ray weak fraction of 24%. In addition, Zappacosta et al. (2020) found 4–5 X-ray weak quasars among 13 hyper luminous RQ quasars at  $z \approx 2$ – $4$ , corresponding to an X-ray weak fraction of  $\approx 30$ – $40\%$ . The definitions of X-ray weak quasars in these studies are slightly different from our adopted  $\Delta\alpha_{\text{OX}} \leq -0.3$  here, but adopting

their definitions would not change significantly the fractions of X-ray weak quasars in our samples and they are still only about 5–7%. There are several factors that may contribute to the discrepancy between the fractions of X-ray weak quasars, and detailed comparison between their result and the Gibson et al. (2008a) sample B result was also presented in Section 5.7 of Nardini et al. (2019). We list two factors below that may be responsible for most of the discrepancy.

1. The fractions among small quasar samples are vulnerable to contamination from a few X-ray weak BAL quasars. There may be missed X-ray weak BAL quasars in the Nardini et al. (2019) and Zappacosta et al. (2020) samples (e.g., Section 5.8 and Appendix B of Nardini et al. 2019), and even one such quasar in the sample would bias the fraction significantly.
2. The fraction of X-ray weak quasars likely has a luminosity dependence, and it becomes larger among more luminous quasars. The main difference between the Nardini et al. (2019) and Zappacosta et al. (2020) samples and our sample is the quasar luminosity. The 29 quasars in Nardini et al. (2019) and 13 quasars in Zappacosta et al. (2020) have a UV luminosity range of  $31.8 \lesssim \log(L_{2500 \text{ \AA}}) \lesssim 32.5$  except one object, while our sample quasars have  $29.3 \lesssim \log(L_{2500 \text{ \AA}}) \lesssim 32.0$ . We do not have a sizable number of very luminous quasars for direct comparison, but if we limit our sample to the 30 most luminous quasars in sample A, which have  $31.4 \lesssim \log(L_{2500 \text{ \AA}}) \lesssim 32.0$  and a median  $\log(L_{2500 \text{ \AA}})$  value of 31.5, the fraction of X-ray weak quasars in this high-luminosity sample becomes  $16 \pm 8\%$ , much larger compared to the fraction in the full sample. If we limit our sample to the 50 most luminous quasars in sample A, which have  $31.3 \lesssim \log(L_{2500 \text{ \AA}}) \lesssim 32.0$  and a median  $\log(L_{2500 \text{ \AA}})$  value of 31.4, the X-ray weak fraction becomes  $15 \pm 6\%$ . Such a luminosity dependence for the fraction of X-ray weak quasars is in general agreement with our interpretations of X-ray weak quasars as WLQs (e.g., Luo et al. 2015; Ni et al. 2018; Section 5.2.1) or due to extreme X-ray variability (e.g., Liu et al. 2019; Ni et al. 2020; Section 5.2.3), where quasars accreting at high Eddington ratios may have X-ray absorption from a geometrically thick inner accretion disk or its associated outflow; the fraction of such quasars is likely higher among more luminous samples. The relevance of the enhanced fraction of X-ray weak quasars to WLQs is also noted in both Nardini et al. (2019) and Zappacosta et al. (2020). We also note that if we divide our sample A into a high-luminosity subsample and a low-

luminosity subsample at the median luminosity of  $\log(L_{2500 \text{ \AA}}) = 30.45$ , the fractions of X-ray weak quasars among the two subsamples are  $6.2 \pm 1.0\%$  and  $5.4 \pm 1.0\%$ , respectively. Such a small difference indicates that the enhanced fraction of X-ray weak quasars (probably related to the enhanced fraction of WLQs) is mostly evident among very luminous quasars.

Given the above comparisons, we stress that the fractions of X-ray weak quasars derived in this study are mostly applicable to quasar samples sharing similar properties to our SDSS quasars here (Table 1), and extra caution is needed if quoting the fractions for quasars with substantially different luminosities.

Finally, we constrain the fraction of intrinsically X-ray weak quasars. In sample B+C, there are nine X-ray weak objects with  $\Gamma_{\text{eff}} \geq 1.26$  (including three with  $\Gamma_{\text{eff}}$  set to 1.8), which we consider to be candidates for intrinsically X-ray weak quasars. Thus, the fraction of intrinsically X-ray weak quasars within the non-BAL quasar population is  $1.4^{+0.8\%}_{-0.4\%} - 2.1^{+0.9\%}_{-0.5\%}$  (6/426–9/426). This fraction would be  $1.2^{+0.8\%}_{-0.3\%} - 1.9^{+0.9\%}_{-0.5\%}$  (5/426–8/426) if we consider X-ray weak objects with  $\Gamma_{\text{eff}} \geq 1.4$  to be candidates for intrinsically X-ray weak quasars. Based on the X-ray properties of 35 Large Bright Quasar Survey (LBQS) BAL quasars, Liu et al. (2018) estimated the fraction of intrinsically X-ray weak quasars within the BAL quasar population to be  $5.7^{+6.7\%}_{-1.9\%} - 23^{+8\%}_{-6\%}$  (2/35–8/35), which is significantly higher than the fraction within the non-BAL quasar population derived here. These results indicate that intrinsically X-ray weak quasars may be preferentially found in BAL quasars (e.g., Luo et al. 2014; Liu et al. 2018), and intrinsically X-ray weak non-BAL quasars like PHL 1811 are extremely rare.

## 5.2. Nature of X-ray Weak Quasars

We discuss the possible nature of the X-ray weak quasars found in this study. We focus on the 26 X-ray weak ( $\Delta\alpha_{\text{OX}} \leq -0.3$ ) quasars in sample B+C (12 in sample B and 14 in sample C), but we also present the overall properties for the X-ray weak quasars in sample A. We consider that there are three types of X-ray weak quasars based on the optical spectral features: WLQs, red quasars, and unclassified X-ray weak quasars. A breakdown of the X-ray weak quasars in samples A and B+C is listed in Table 5.

### 5.2.1. X-ray Weak WLQs

With a large fraction ( $\gtrsim 50\%$ ) of quasars showing weak X-ray emission, WLQs represent one population of X-ray weak quasars (e.g., Wu et al. 2012; Luo et al. 2015; Ni et al. 2018; Timlin et al. 2020). X-ray weak WLQs were also found to have average small effective photon index, suggestive of X-ray absorption (e.g., Luo



**Table 5.** Numbers of Potentially Absorbed and Unabsorbed Quasars in the X-ray Weak Populations

X-ray Weak Population	Sample A					Sample B+C			
	Undetected	Detected				Detected			
		All	All	Abs.	Unabs.	Unclear	All	Abs.	Unabs.
WLQ <sup>a</sup>	1	9	6	2	1	7	4	2	1
Red quasar <sup>b</sup>	1	13	10	1	2	8	6	0	2
Red WLQ	1	3	2	0	1	3	2	0	1
Red non-WLQ	0	10	8	1	1	5	4	0	1
Unclassified <sup>c</sup>	0	45	37	7	1	14	9	4	1
Total	1	64	51	10	3	26	17	6	3

NOTE—We adopted  $\Delta\alpha_{\text{OX}} = -0.3$  to be the threshold separating X-ray normal and X-ray weak quasars (Section 4.2). All the undetected X-ray weak quasars in sample A have fixed X-ray photon indices of  $\Gamma_{\text{eff}} = 1.8$ ; the numbers of detected X-ray weak quasars with fixed  $\Gamma_{\text{eff}}$  values of 1.8 (see Section 3) are listed in the “Unclear” columns.

<sup>a</sup>We adopted  $C\text{ IV REW} = 16\text{ \AA}$  to be the threshold separating WLQs and normal quasars (Section 5.2.1).

<sup>b</sup>We adopted  $\Delta(g-i) = 0.2$  to be the threshold separating red and normal quasars (Section 5.2.2).

<sup>c</sup>We consider an X-ray weak quasar to be in the unclassified population if it is neither a WLQ nor a red quasar (Section 5.2.3).

et al. 2015). Their X-ray emission may be absorbed by “shielding gas” (e.g., Wu et al. 2011, 2012) or a geometrically thick inner accretion disk (e.g., Luo et al. 2015; Ni et al. 2018, 2020).

There is no uniform definition for WLQs. For high-redshift ( $z > 2.200$ ) quasars, WLQs are generally selected using the REW of the  $\text{Ly}\alpha + \text{N V}$  emission lines. Shemmer et al. (2009) defined WLQs to be quasars with  $\text{Ly}\alpha + \text{N V REW} < 10\text{ \AA}$ ; Diamond-Stanic et al. (2009) defined WLQs to be those with  $\text{Ly}\alpha + \text{N V REW} < 15.4\text{ \AA}$  ( $> 3\sigma$  deviation from the mean of the log-normal distribution). For low-redshift ( $z \leq 2.200$ ) quasars, which do not have  $\text{Ly}\alpha + \text{N V}$  coverage in their optical spectra, the definition of WLQs is commonly based on other strong emission lines (e.g.,  $C\text{ IV}$ ,  $C\text{ III]$ ,  $\text{Mg II}$ , and  $\text{H}\beta$ ). Wu et al. (2012) and Luo et al. (2015) selected WLQs from the Plotkin et al. (2010b) catalog, which has  $\text{REW} \lesssim 5\text{ \AA}$  for all emission features. Recently, Ni et al. (2018) called quasars with  $C\text{ IV REW} < 7.0\text{ \AA}$  “extreme” WLQs, and quasars with  $C\text{ IV REW} = 7.0\text{--}15.5\text{ \AA}$  “bridge” WLQs, which have emission-line features in between those of extreme WLQs and typical quasars.

The  $C\text{ IV REW}$  values of our 26 X-ray weak quasars in sample B+C range from 6.6 to 56.8  $\text{\AA}$ , with a median value of 24.4  $\text{\AA}$  and a mean value of 25.6  $\text{\AA}$ . We adopted  $C\text{ IV REW} = 16\text{ \AA}$  to be the threshold separating WLQs and normal quasars in this paper. Our more inclusive definition  $C\text{ IV REW} < 16\text{ \AA}$  for WLQs corresponds to a  $> 2.0\sigma$  deviation from the mean of the

log-normal distribution for SDSS quasars, where the distribution of  $C\text{ IV REW}$  shows an apparent tail toward small values (see Section 3.2 of Wu et al. 2012). Since all of our sample objects have  $C\text{ IV}$  coverage, we consider this criterion appropriate for this study. For any sample object that has both SDSS DR7 and BOSS DR10 spectra, we consider it a WLQ if either spectrum has  $C\text{ IV REW} < 16\text{ \AA}$ . Given this criterion, sample B+C contains seven X-ray weak WLQs. Figure 8 shows the spectra of these seven quasars. We note that three of them (J1219+1244, J1350+2618, and J1457+2218) have both SDSS DR7 and BOSS DR10 spectra. For J1219+1244 and J1350+2618, all their spectra satisfy the WLQ criterion, while for J1457+2218, only its BOSS DR10 spectrum does.

Given our WLQ definition of  $C\text{ IV REW} < 16\text{ \AA}$ , sample B+C contains 20 WLQs, seven of which are X-ray weak, corresponding to an X-ray weak fraction of  $35_{-9}^{+12}\%$ . The seven X-ray weak WLQs have a comparable  $C\text{ IV REW}$  distribution to the other 13 X-ray normal WLQs; e.g., the median  $C\text{ IV REW}$ s are 11.9 and 9.2  $\text{\AA}$ , respectively. By contrast, the fraction of X-ray weak quasars is only  $4.7_{-0.8}^{+1.3}\%$  (19/406) among the non-WLQs in sample B+C. Thus, WLQs show significantly higher X-ray weak fraction when compared to non-WLQs. These results confirm previous findings that WLQs represent one population of X-ray weak quasars (e.g., Wu et al. 2012; Luo et al. 2015; Ni et al. 2018).

Ni et al. (2018) investigated a sample of 32 WLQs selected mainly from the Shen et al. (2011) and Plotkin

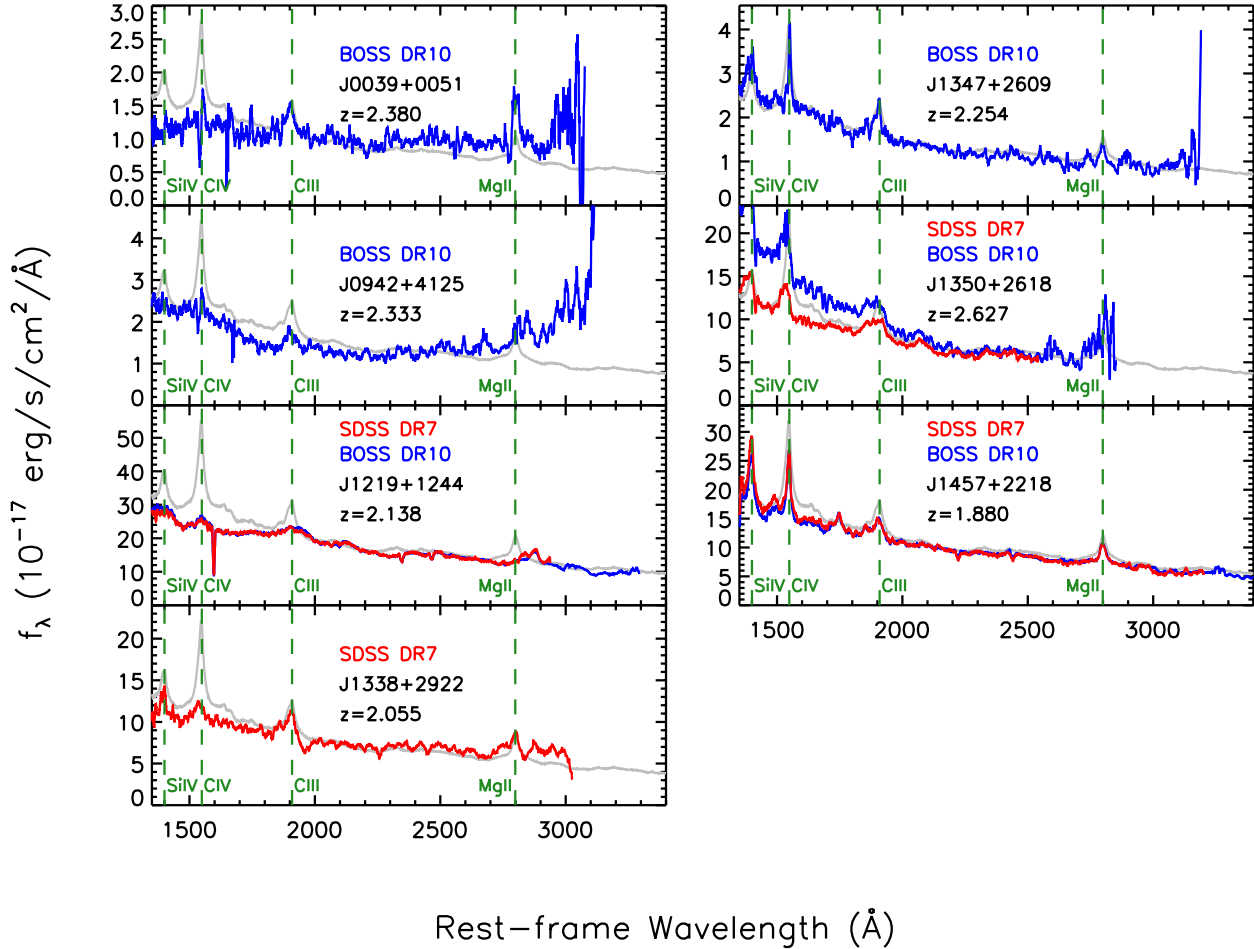


**Figure 8.** SDSS optical/UV spectra (smoothed by a 20 pixel boxcar) for the seven X-ray weak WLQs (red curves for SDSS DR7 spectra and blue curves for BOSS DR10 spectra). The gray curve in each panel shows the SDSS composite quasar spectrum (Vanden Berk et al. 2001) for comparison. SDSS Data Release number, name, and redshift for each object are listed.

et al. (2010b) catalogs. They adopted a definition of C IV REW  $< 15.5 \text{ \AA}$  for “extreme”+“bridge” WLQs, which is similar to our WLQ definition, and the fraction of X-ray weak objects within their WLQ sample is  $44_{-8}^{+9}\%$  (14/32). We note that Ni et al. (2018) adopted  $\Delta\alpha_{\text{OX}} < -0.2$  to define X-ray weak quasars. If we use this same definition, sample B+C would contain ten X-ray weak WLQs and the X-ray weak fraction for WLQs would be  $50 \pm 11\%$ , which is in agreement with Ni et al. (2018).

Wu et al. (2011) proposed a “shielding gas” scenario to unify X-ray normal and X-ray weak WLQs. In this scenario, a small fraction of the quasar population has high-ionization shielding gas lying between the SMBH and the broad emission-line region (BELR). With high column density and large BELR covering factor, the shielding gas is able to prevent most, if not all, X-ray emission and other ionizing continuum from reaching the BELR. If such a quasar is viewed through the shielding gas, an X-ray weak WLQ is seen; if it is viewed from other orientations, an X-ray normal WLQ is seen. The aver-

age hard X-ray spectrum via stacking analyses, which is suggestive of X-ray absorption, further supports the shielding-gas scenario (Luo et al. 2015).

The  $\Gamma_{\text{eff}}$  values of the seven X-ray weak WLQs in sample B+C are listed in Table 6. Given our  $\Gamma_{\text{eff}} < 1.26$  criterion for being potentially X-ray absorbed (Section 4.1), four of the seven X-ray weak WLQs are potentially X-ray absorbed, with their  $\Gamma_{\text{eff}}$  values ranging from  $-0.8$  to  $1.1$ . The small effective photon indices for these four X-ray absorbed WLQs are consistent with the shielding-gas scenario (e.g., Wu et al. 2011, 2012). In addition, there are two apparently unabsorbed X-ray weak WLQs, J1350+2618 and J1457+2218, which have  $\Gamma_{\text{eff}} = 2.0_{-1.0}^{+1.9}$  and  $1.6_{-0.2}^{+0.3}$ , respectively. These two are good candidates for intrinsically X-ray weak quasars. One of them, J1457+2218, is detected in all three X-ray bands. With 70 photons in the broad band, it is the only object that has  $> 50$  broad-band photons in sample B+C. We present X-ray spectral analysis of J1457+2218 in Appendix A. Another quasar, J1219+1244, is undetected in both the soft and hard bands and has a fixed

**Table 6.** Broad-band Counts and  $\Gamma_{\text{eff}}$  Values for the X-ray Weak WLQs in Sample B+C

Object	Broad-band	
	Counts	$\Gamma_{\text{eff}}$
J003927.13 + 005152.8	2	$-0.8^{+1.4}_{-3.3}$
J094200.66 + 412545.3	7	$-0.4 \pm 1.0$
J121946.20 + 124454.1 <sup>a</sup>	2	1.8
J133820.04 + 292206.1	17	$1.1^{+0.9}_{-1.0}$
J134745.49 + 260940.1	22	$1.0 \pm 0.4$
J135058.12 + 261855.2	10	$2.0^{+1.9}_{-1.0}$
J145710.80 + 221844.8	70	$1.6^{+0.3}_{-0.2}$

NOTE—We adopted C IV REW = 16 Å for the threshold separating WLQs and normal quasars in this paper.

<sup>a</sup>J1219 + 1244 is undetected in both the soft and hard bands and has a fixed X-ray photon index of  $\Gamma_{\text{eff}} = 1.8$ .

photon index of  $\Gamma_{\text{eff}} = 1.8$ , and thus it is unclear whether this object is X-ray absorbed.

However, we note that, except for J1457+2218, the other six X-ray weak WLQs have only 2–22 photons in the broad band, leading to substantial uncertainties of the effective photon indices  $\Gamma_{\text{eff}}$  (see Table 6). We also note that four X-ray weak WLQs (J0039+0051, J1219+1244, J1347+2609, and J1350+2618) are mini-BAL quasars (see Section 5.2.3 below), and their X-ray weakness might also be related to their mini-BAL features, although mini-BALs do not necessarily lead to weak X-ray emission.

Based on the Wu et al. (2011) shielding-gas scenario, Luo et al. (2015) proposed that the shielding gas may be a geometrically thick inner accretion disk. When a quasar is accreting at a high Eddington ratio ( $L_{\text{Bol}}/L_{\text{Edd}} \gtrsim 0.3$ ), its inner accretion disk may become significantly puffed up (e.g., Koratkar & Blaes 1999; Blaes et al. 2001; Laor & Davis 2011; Slone & Netzer 2012; Netzer & Trakhtenbrot 2014). The puffed-up disk can block nuclear X-rays and other ionizing photons from reaching an equatorial BELR. Thus, an X-ray weak WLQ can be seen when such a quasar is viewed through the thick inner disk.

To test the Luo et al. (2015) model, we estimated the  $L_{\text{Bol}}/L_{\text{Edd}}$  values of our sample objects from their bolometric luminosities and SMBH masses. We measured SMBH masses using the Mg II (Vestergaard & Osmer 2009) or C IV (Vestergaard & Peterson 2006) virial estimator. We preferred Mg II-based estimates to C IV-based estimates when calculating the SMBH masses, because the C IV virial estimator is more un-

certain. We calculated the bolometric luminosities as  $L_{\text{Bol}} = 5.15\lambda L_{\lambda}(3000\text{\AA})$  for Mg II-based estimates or  $L_{\text{Bol}} = 3.81\lambda L_{\lambda}(1350\text{\AA})$  for C IV-based estimates (Shen et al. 2011). Of the seven X-ray weak WLQs in sample B+C, all but one (J1350+2618) have Mg II-based virial SMBH masses.

The  $L_{\text{Bol}}/L_{\text{Edd}}$  values of our seven X-ray weak WLQs in sample B+C range from 0.06 to 0.79, with a median value of 0.16. A Kolmogorov-Smirnov test indicates no significant difference between the  $L_{\text{Bol}}/L_{\text{Edd}}$  values for the seven X-ray weak WLQs and the 406 non-WLQs in sample B+C ( $p = 0.44$ ), which does not support the high  $L_{\text{Bol}}/L_{\text{Edd}}$  scenario for WLQs. However, we note that the Mg II- or C IV-based virial masses are less reliable as compared to H $\beta$ -based virial masses, and the systematic uncertainties associated with the virial estimates might be as large as  $\gtrsim 0.4$  dex (e.g., Shen et al. 2011). Furthermore, virial estimates are most likely to fail at high Eddington ratios (e.g., Marconi et al. 2008, 2009; Netzer & Marziani 2010). Thus, the  $L_{\text{Bol}}/L_{\text{Edd}}$  values derived from Mg II- or C IV-based estimates may be highly uncertain. Near-infrared spectroscopy covering the H $\beta$  line is needed to provide more accurate  $L_{\text{Bol}}/L_{\text{Edd}}$  estimates.

In sample A, there are 60 WLQs, 35 of which are X-ray detected and 25 of which are X-ray undetected. Utilizing the Kaplan-Meier estimator in ASURV, we found the X-ray weak fraction within the 60 WLQs to be  $35 \pm 8\%$ , which is consistent with that derived from sample B+C. Of the nine detected X-ray weak WLQs in sample A, six are likely X-ray absorbed with  $\Gamma_{\text{eff}}$  values ranging from  $-0.8$  to  $1.1$ , and two (both included in sample B+C) are potentially X-ray unabsorbed. The other WLQ (included in sample B+C) is undetected in both the soft and hard bands, and thus it is unclear if it is X-ray absorbed.

### 5.2.2. X-ray Weak Red Quasars

In addition to WLQs, there exists a population of red type 1 quasars that can be X-ray weak (e.g., Wilkes et al. 2005; Hall et al. 2006). Previous X-ray studies have demonstrated that quasars with the reddest optical colors at their redshifts are more likely to be X-ray absorbed than typical quasars (e.g., Wilkes et al. 2005), although some of the reddest quasars may show no evidence of X-ray absorption or X-ray weakness (e.g., Hall et al. 2006). These optically red quasars may be X-ray obscured by dusty gas, which also extinguishes the UV continuum, perhaps from a starburst disk surrounding their accreting SMBHs (e.g., Hickox & Alexander 2018).

Broadband photometric studies of SDSS quasars have revealed a strong dependence of quasar optical/UV colors upon redshift (e.g., Richards et al. 2001), and the relative  $g - i$  color,  $\Delta(g - i)$ , is a useful redshift-independent indicator of the optical/UV spectral shape (e.g., Richards et al. 2003). For a quasar at a given redshift,  $\Delta(g - i)$  is defined as the difference between the  $g - i$  color of that quasar and the modal  $g - i$  value

of quasars at that redshift.  $\Delta(g-i) > 0$  indicates a redder-than-average continuum, while  $\Delta(g-i) < 0$  indicates a bluer-than-average continuum. The  $\Delta(g-i)$  distribution for SDSS quasars is roughly Gaussian but has a distinct red tail with  $\Delta(g-i) \gtrsim 0.2$ , which is indicative of dust reddening (Richards et al. 2003). Based on the  $\Delta(g-i)$  distribution, Hall et al. (2006) adopted  $\Delta(g-i) > 0.2$  to select red quasars for X-ray study.

The  $\Delta(g-i)$  values of the 26 X-ray weak quasars in our sample B+C range from  $-0.20$  to  $0.82$ , with a median value of  $0.11$  and a mean value of  $0.17$ . Following Hall et al. (2006), we adopted  $\Delta(g-i) = 0.2$  to be the threshold separating red and normal quasars in this paper. Given this criterion, sample B+C contains eight X-ray weak red quasars, with  $\Delta(g-i)$  values ranging from  $0.29$  to  $0.82$ . We note that although the  $\Delta(g-i) > 0.2$  criterion was designed to select dust-reddened quasars, the possibility of selecting unreddened quasars (with intrinsically red continua) cannot be entirely excluded. However, given that all our X-ray weak red quasars in sample B+C have  $\Delta(g-i) \gtrsim 0.3$ , they are likely to be dominated by dust-reddened quasars (e.g., Richards et al. 2003; Hall et al. 2006; Krawczyk et al. 2015).

Given our red quasar definition of  $\Delta(g-i) > 0.2$ , sample B+C contains 63 red quasars, eight of which are X-ray weak, corresponding to an X-ray weak fraction of  $13_{-3}^{+5}\%$ . By contrast, only  $5.0_{-0.9}^{+1.4}\%$  ( $18/363$ ) of non-red quasars are X-ray weak. If we exclude red WLQs, the X-ray weak fraction for red and non-red quasars within sample B+C are  $9.3_{-2.6}^{+5.5}\%$  ( $5/54$ ) and  $4.0_{-0.8}^{+1.3}\%$  ( $14/352$ ), respectively. These results suggest that red quasars are likely to be another population of X-ray weak quasars in addition to WLQs, although red quasars apparently have a smaller X-ray weak fraction than WLQs.

Of the eight X-ray weak red quasars, three (J0039+0051, J1219+1244 and J1338+J2922) are red WLQs with C IV REW  $< 12 \text{ \AA}$ . J0039+0051 and J1338+J2922 are likely X-ray absorbed with  $\Gamma_{\text{eff}} = -0.8_{-3.3}^{+1.4}$  and  $1.1_{-1.0}^{+0.9}$ , respectively. Interestingly, J0039+0051 is the reddest ( $\Delta(g-i) = 0.82$ ) X-ray weak quasar in sample B+C, while J1338+J2922 has the highest Eddington ratio ( $L_{\text{Bol}}/L_{\text{Edd}} = 0.79$ ; see Section 5.2.1) among X-ray weak WLQs in sample B+C. The other object, J1219+1244, has a fixed photon index of  $\Gamma_{\text{eff}} = 1.8$  (see Section 5.2.1).

Of the remaining five X-ray weak red quasars, four are likely X-ray absorbed, as their  $\Gamma_{\text{eff}}$  values range from  $-1.2$  to  $1.1$ . The other quasar, J1522+0836, is undetected in both the soft and hard bands and has a fixed photon index of  $\Gamma_{\text{eff}} = 1.8$ . Since dust causes optical/UV reddening and gas causes X-ray absorption, the reddened optical/UV color together with absorbed X-ray emission indicate that these X-ray weak red quasars may have optical/UV and X-ray absorption from dusty gas (Hall et al. 2006), perhaps from a starburst disk (e.g., Thompson et al. 2005; Ballantyne 2008).

We note that J1002+0203, the second reddest ( $\Delta(g-i) = 0.74$ ) X-ray weak quasar in sample B+C, shows relatively weak C IV emission with REW =  $19 \text{ \AA}$  (although not satisfying our WLQ criterion). It has 27 broad-band counts and is detected in all three X-ray bands. J1002+0203 has a small photon index of  $\Gamma_{\text{eff}} = 1.1$  and a high Eddington ratio of  $L_{\text{Bol}}/L_{\text{Edd}} = 0.59$ . Thus, the X-ray weakness of this quasar might also be explained via the thick inner disk scenario for WLQs (e.g., Luo et al. 2015; Ni et al. 2018).

Although their small  $\Gamma_{\text{eff}}$  values suggest X-ray absorption, these X-ray weak red quasars have only 2–27 photon counts in the broad band, and thus the uncertainties on the effective photon indices  $\Gamma_{\text{eff}}$  are large. In addition, there are five X-ray weak red quasars (J0039+0051, J0228+0040, J1219+1244, J1239+1221, and J1522+0836) that are mini-BAL quasars (see Section 5.2.3 below), and their X-ray weakness might also be related to their mini-BAL features, although mini-BALs do not necessarily cause weak X-ray emission.

In sample A, there are 193 red quasars, 147 of which are X-ray detected and 46 of which are X-ray undetected. Utilizing the Kaplan-Meier estimator in ASURV, we found the X-ray weak fraction within the 193 red quasars to be  $12 \pm 3\%$ , which is consistent with that derived from sample B+C. Of the ten detected X-ray weak red non-WLQs in sample A, eight are likely X-ray absorbed and their  $\Gamma_{\text{eff}}$  values range from  $-1.2$  to  $1.1$ . Another one (J1237+6203; not included in sample B+C) is potentially X-ray unabsorbed with  $\Gamma_{\text{eff}} = 1.6 \pm 0.4$ . Its large  $\Gamma_{\text{eff}}$  value suggests that this red non-WLQ is a candidate for an intrinsically X-ray weak quasar. The other one (J1522+0836; included in sample B+C) is undetected in both the soft and hard bands, and thus it is unclear whether this object is X-ray absorbed.

### 5.2.3. Unclassified X-ray Weak Quasars

In addition to the seven WLQs and five red non-WLQs, there are another 14 objects in sample B+C that are X-ray weak. They do not have substantially unusual spectral features like WLQs or red quasars, and the reasons for their X-ray weakness remain unclear. We consider an X-ray weak quasar that is neither a WLQ nor a red quasar to be in the unclassified category (see Table 5). Figure 9 shows the SDSS spectra of the 14 unclassified X-ray weak quasars in sample B+C. We proceed by enumerating some possible explanations for their weak X-ray emission.

1. One possible explanation for their X-ray weakness is relatively weak C IV line emission. There are five X-ray weak objects (J0050–0054, J0157–0056, J0941+3946, J1235+2805, and J1629+2319) in the unclassified category that have C IV REW ranging from  $16$  to  $25 \text{ \AA}$ . Their relatively weak emission lines (although not satisfying our WLQ



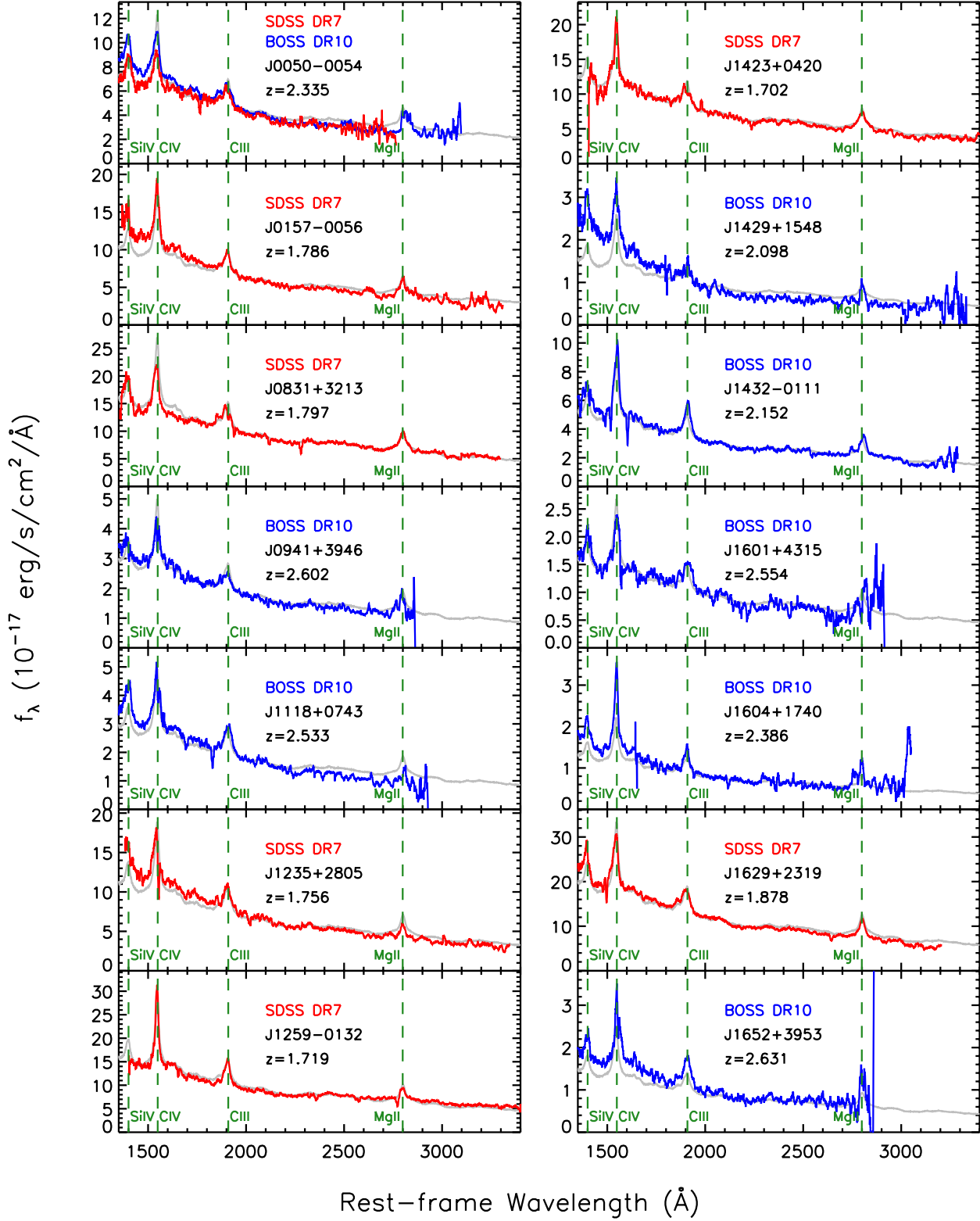


**Figure 9.** SDSS optical/UV spectra (smoothed by a 20 pixel boxcar) for the 14 X-ray weak quasars in the unclassified category (red curves for SDSS DR7 spectra and blue curves for BOSS DR10 spectra). The gray curve in each panel shows the SDSS composite quasar spectrum (Vanden Berk et al. 2001) for comparison. SDSS Data Release number, name, and redshift for each object are listed.

definition of C IV REW  $< 16 \text{ \AA}$ ) may explain their X-ray weakness following Section 5.2.1. However, we note that a relatively weak C IV emission line does not necessarily lead to weak X-ray emission. For example, of the 46 quasars with C IV REW between 16 and 25  $\text{\AA}$  in Sample B+C, 37 ( $80^{+5}_{-7}\%$ ) are X-ray normal (see also section 5.2 of Ni et al. 2018). Therefore, it is just one possibility that the X-ray weakness of these five objects may be related to their relatively weak C IV emission lines.

2. The second explanation is relatively red optical/UV color following Section 5.2.2. One unclassified X-ray weak object, J1259–0132, has  $\Delta(g - i) = 0.11$ . Visual inspection of its SDSS spectrum (see Figure 9) confirmed that J1259–0132 has a slightly redder-than-average continuum, which may explain its X-ray weakness. We note that like the relatively weak C IV emission line, a relatively red continuum does not necessarily cause weak X-ray emission either. For example, of the 29 quasars with  $0.1 < \Delta(g - i) < 0.2$  and visually confirmed redder-than-average continua in sample B+C, 27 ( $93^{+2}_{-8}\%$ ) are X-ray normal.
3. Another possible explanation is mini-BALs, which are absorption features in between those of the traditional BALs (trough width  $\geq 2,000 \text{ km s}^{-1}$ ) and narrow absorption lines (NALs; trough width  $< 500 \text{ km s}^{-1}$ ). Mini-BAL quasars have  $\Delta\alpha_{\text{OX}}$  values intermediate between those of BAL and non-BAL quasars (e.g., Gibson et al. 2009b; Wu et al. 2010), and some of them show X-ray absorption similar to that of BAL quasars (e.g., Gallagher et al. 2002).

Since we adopted the Trump et al. (2006)  $\text{AI} > 0$  definition (see Section 2.2), which requires a minimum trough width of  $1,000 \text{ km s}^{-1}$ , to identify BAL features, we defined mini-BALs using the following equation:

$$\text{AI}_{\text{mini}} \equiv \int_0^{29,000} (1 - f(v))C' dv. \quad (4)$$

Similar to the AI definition, in this equation  $f(v)$  is the continuum-normalized flux density, and the value of  $C'$  is initially set to zero; it is set to 1 whenever the  $f(v)$  has been continuously less than 0.9 for a trough width of  $500 - 1,000 \text{ km s}^{-1}$ . Wu et al. (2010) suggested that mini-BALs with trough widths of  $500 - 1,000 \text{ km s}^{-1}$  appear to be related to  $\Delta\alpha_{\text{OX}}$ . We consider a sample object with  $\text{AI}_{\text{mini}} > 0$  a mini-BAL quasar. There are five unclassified X-ray weak quasars (J1423+0420, J1432–0111, J1601+4315, J1629+2319,<sup>10</sup> and

J1652+3953) in sample B+C that are mini-BAL quasars, and their X-ray weakness may be explained by their mini-BAL features. However, we caution that it is just one possibility that the X-ray weakness of these five objects may be related to their mini-BAL features, as mini-BAL quasars do not appear to be an X-ray weak population in general. For example, among the 156 mini-BAL quasars in sample B+C given our adopted definition, 144 ( $92^{+2}_{-3}\%$ ) are X-ray normal.

4. The fourth possible explanation is NALs. Visual inspection of the SDSS spectra (see Figure 9) indicated that J1118+0743 appears to exhibit narrow Al III  $\lambda 1857$  absorption. Its X-ray weakness may be ascribed to absorption, although like mini-BALs, NAL features do not necessarily lead to weak X-ray emission either (e.g., Ganguly et al. 2001).
5. The fifth explanation is X-ray variability, and we consider this the most plausible explanation for the majority of the unclassified X-ray weak quasars. Such variable quasars may include quasars that vary strongly in the X-ray band but not in the optical/UV, “changing-look” quasars, and quasars that show BAL disappearance or emergence.

Although most type 1 quasars show X-ray variability by factors of less than two (e.g., Yang et al. 2016), there is a rare population of extremely X-ray variable quasars (e.g., PG 1211+143: Bachev et al. 2009; PG 0844+349: Gallo et al. 2011; Gibson & Brandt 2012; PHL 1092: Miniutti et al. 2012; Liu et al. 2019; Timlin et al. 2020) which can vary by factors of larger than 10 in X-rays but show little variation in the optical/UV bands. They become remarkably X-ray weak in the low X-ray flux state, and their X-ray weakness may be due to partial-covering absorption or inner-disk reflection (e.g., Bachev et al. 2009; Gallo et al. 2011; Miniutti et al. 2012; Liu et al. 2019; Ni et al. 2020). We note that such X-ray variability is not expected to have an X-ray strong state, consistent with observations to date.

There also exist a few “changing-look” quasars that show strong long-term flux variability in both the optical/UV and X-ray bands (e.g., LaMassa et al. 2015). If we calculate their  $\alpha_{\text{OX}}$  values based on non-simultaneous X-ray and optical/UV observations, we may consider them to be X-ray weak quasars whenever their X-ray dim states are combined with optically bright states. Conversely, such quasars may become X-ray strong if their X-ray bright states are combined with optically dim states.

<sup>10</sup> J1629+2319 has a relatively weak C IV emission line with REW = 24  $\text{\AA}$ , which may also explain its X-ray weakness.

**Table 7.** SDSS and *Chandra* Observational Dates for Unclassified X-ray Weak Quasars in Sample B+C

SDSS Name	SDSS Date	<i>Chandra</i> Date	Rest-frame	
			Separation (year)	
005018.84 – 005438.0	10/17/2001	09/02/2004	0.8	
015704.11 – 005657.5	10/17/2001	11/27/2014	4.4	
083116.62 + 321329.6	12/12/2002	12/22/2007	1.8	
094138.06 + 394630.2	03/09/2011	01/16/2008	1.1	
111828.31 + 074300.1	01/03/2012	01/31/2008	1.4	
123559.06 + 280550.9	12/25/2005	01/14/2001	1.8	
125923.50 – 013234.9	05/30/2000	02/28/2009	3.1	
142339.87 + 042041.1	05/20/2001	12/15/2012	3.8	
142921.75 + 154841.4	04/18/2012	12/06/2013	0.5	
143212.69 – 011109.7	02/26/2011	03/31/2000	3.2	
160154.45 + 431519.6	06/18/2012	10/07/2003	3.2	
160408.26 + 174042.4	05/22/2010	07/25/2004	2.1	
162922.87 + 231958.2	08/09/2004	10/20/2013	3.0	
165209.44 + 395348.8	05/27/2012	05/19/2014	0.7	

There is another rare population of quasars showing emerging or disappearing BALs (e.g. McGraw et al. 2017; De Cicco et al. 2018; Rogerson et al. 2018; Sameer et al. 2019). These objects may be considered X-ray weak quasars if they are non-BAL quasars when their optical/UV data are taken, but happen to exhibit BAL features, which cause weak X-ray emission, when their X-ray data are taken. The frequency of such highly variable X-ray absorption in quasars with emerging or disappearing BALs is presently poorly constrained. There is no X-ray strong state for this variability.

The SDSS and *Chandra* observation dates for the 14 sample B+C objects in the unclassified X-ray weak category are listed in Table 7. It is clear that their SDSS optical/UV spectra and *Chandra* X-ray data are not simultaneous but separated by  $\approx 1$ –4 years in the rest frame. Thus, their X-ray weakness is possibly due to X-ray and/or optical/UV spectral variability effects. Based on over 15,000 SDSS quasars at  $z > 1.680$  matched between DR7 and DR9+DR10, Rogerson et al. (2018) studied the emergence and disappearance of BAL features. They estimated the fraction of non-BAL quasars turning into BAL quasars to be  $0.59\% \pm 0.12\%$  over timescales of 1–3 years in the rest frame. As the time separations between the X-ray and optical/UV observations for our sample B+C objects are comparable to the timescales of BAL variability studied in Rogerson et al. (2018), we expect to see 2–3 sample B+C quasars exhibiting non-BAL-to-BAL transitions, probably included in the 14 unclassified X-ray weak objects.

Given our definition of potentially X-ray absorbed quasars ( $\Gamma_{\text{eff}} < 1.26$ ), nine of these 14 unclassified X-ray weak quasars are likely X-ray absorbed, with their  $\Gamma_{\text{eff}}$  values ranging from  $-0.4$  to  $1.0$ . Four quasars (J1118+0743, J1429+1548, J1601+4315, and J1629+2319) are potentially X-ray unabsorbed with  $\Gamma_{\text{eff}} = 1.3 \pm 0.50$ ,  $1.4_{-0.6}^{+0.7}$ ,  $2.1_{-1.3}^{+1.0}$ , and  $2.3_{-1.4}^{+0.9}$  respectively; these are candidates for intrinsically X-ray weak quasars. The remaining quasar, J0941+3946, is undetected in both the soft and hard bands, and thus it is unclear whether this object is X-ray absorbed. We caution that these 14 unclassified X-ray weak quasars have only 2–19 photon counts in the broad band, leading to substantial uncertainties on their  $\Gamma_{\text{eff}}$  values.

In sample A, there are 45 unclassified X-ray weak quasars, nine of which have relatively weak emission lines with C IV REW ranging from 16 to 25 Å, two of which have  $0.1 < \Delta(g - i) < 0.2$  and visually confirmed redder-than-average continua, and 12 of which are mini-BAL quasars. All these 45 unclassified X-ray weak quasars are X-ray detected. Among these quasars, 37 are likely X-ray absorbed with  $\Gamma_{\text{eff}}$  values ranging from  $-1.4$  to  $1.2$ , and seven (three not included in sample B+C) are potentially X-ray unabsorbed, with their  $\Gamma_{\text{eff}}$  values ranging from 1.3 to 2.3. These seven objects are candidates for intrinsically X-ray weak quasars. The other quasar (included in sample B+C) is undetected in both the soft and hard bands, and thus it is unclear if this object is X-ray absorbed.

## 6. SUMMARY AND FUTURE WORK

We have investigated systematically the X-ray properties of a large sample of SDSS quasars. We constrained the fraction of X-ray weak quasars, and discussed the possible causes of quasar X-ray weakness. The main points from this work are the following:

1. After removal of BAL and RL quasars, we selected the final sample, or sample A, of 1825 SDSS DR7 and DR10 quasars with *Chandra* archival X-ray observations (Section 2). We measured their X-ray properties (Section 3), calculated the  $\alpha_{\text{OX}}$  parameter, and investigated the  $\alpha_{\text{OX}} - L_{2500 \text{ \AA}}$  relation (Section 4.1).
2. The  $\Delta\alpha_{\text{OX}}$  distribution for sample A has a clear negative tail, suggesting the existence of a population of X-ray weak quasars. The fraction of X-ray weak quasars ( $\Delta\alpha_{\text{OX}} \leq -0.3$ ) is  $5.8 \pm 0.7\%$ , and quasars that are X-ray weak by factors of 10 and 20 represent  $2.7 \pm 0.5\%$  and  $1.3 \pm 0.3\%$  of the population, respectively. See Section 4.2.
3. We constructed two subsamples (samples B and C), without direct reference to their X-ray properties, that contain 218 DR7 and 208 DR10 quasars, respectively. Both subsamples are composed of

X-ray detections only, and the fractions of X-ray weak quasars among these two subsamples are consistent with that in sample A. See Section 4.3.

4. We note that the fraction of X-ray weak quasars likely has a luminosity dependence. The fractions derived in this study are mostly applicable to quasar samples sharing similar properties to our SDSS quasars here (Table 1), and extra caution is needed if quoting the fractions for quasars with substantially different luminosities. See Section 5.1.
5. WLQs ( $C\text{ IV REW} < 16\text{ \AA}$ ) represent one population of X-ray weak quasars, and their X-ray weak fraction ( $35_{-9}^{+12}\%$ ) is significantly higher than that of non-WLQs. See Section 5.2.1.
6. Red quasars ( $\Delta(g-i) > 0.2$ ) are likely to be another population of X-ray weak quasars, and their X-ray weak fraction ( $13_{-3}^{+5}\%$ ) is considerably higher than that of normal quasars. See Section 5.2.2.
7. We provide several possible explanations for the X-ray weakness of quasars in the unclassified category: relatively weak  $C\text{ IV}$  emission lines, relatively red optical/UV continua, mini-BALs, NALs, and X-ray variability. We consider X-ray variability the most plausible explanation; such quasars include quasars that vary strongly in the X-ray band but not in the optical/UV, “changing-look” quasars, and quasars that show BAL disappearance or emergence. See Section 5.2.3.

Further work is needed to improve the results of this study. Deeper radio observations, e.g., with the Very Large Array Sky Survey (VLASS, e.g., Lacy et al. 2019, 2020) will be helpful to discriminate  $R \geq 10$  vs.  $R < 10$  for the optically faint quasars (especially the post-DR7 quasars), thus removing non-RQ objects with possibly enhanced X-ray emission. Deeper X-ray observations, e.g., *Chandra* observations with typical individual exposure times of  $\approx 30$  ks (estimated from the current median exposure time and source counts) are required to better constrain the spectral shapes of the detected sources, thus helping distinguish more reliably between absorbed and unabsorbed quasars.

Additionally, although X-ray weak quasars constitute only a small fraction of the non-BAL quasar population, they may provide us with new insights into the SMBH disk-corona system and BELR. Deeper targeted X-ray observations of our X-ray weak quasars, especially those candidates for intrinsically X-ray weak quasars and unclassified X-ray weak quasars, are necessary to assess

their physical nature. For example, *Chandra* observations with exposure times of  $\approx 100$  ks will on average yield  $\approx 50$  broad-band counts for the X-ray weak quasars in sample B+C.

Our study here will benefit from a larger sample of X-ray quasars, to increase the statistical significance of the results and to identify more X-ray weak quasars. The SDSS Data Release 16 quasar catalog (DR16Q; Lyke et al. 2020) contains 750,426 spectroscopically confirmed quasars. Combining the *Chandra* archive with the DR16Q will extend the X-ray quasar study to an even larger sample. Furthermore, the *XMM-Newton* serendipitous source catalogs (e.g., Watson et al. 2009; Rosen et al. 2016) are good complements to the *Chandra* archival X-ray data. The latest 4XMM-DR9 catalog covers a sky area of  $1152\text{ deg}^2$ , and contains 810,795 detections comprising 550,124 unique X-ray sources.<sup>11</sup> With an estimated 20,000–25,000 matches in the DR16Q catalog, the 4XMM-DR9 catalog can significantly increase the number of X-ray quasars.

Finally, *eROSITA* (extended ROentgen Survey with an Imaging Telescope Array; Merloni et al. 2012), a Russian-German space mission, will discover many more X-ray AGNs and quasars in the near future.<sup>12</sup> Launched on 13 July 2019, *eROSITA* is performing a medium-depth X-ray all-sky survey over the next four years. *eROSITA* is to map the entire sky in the soft X-ray band (0.5–2 keV) at a level  $> 20$  times more sensitive than the *ROSAT* all sky survey, as well as in the hard X-ray band (2–10 keV) which provides the first imaging all sky survey at these higher X-ray energies. The 4-year *eROSITA* all-sky survey is expected to detect  $\approx 3$  million AGNs and quasars. However, the expected sensitivity of the 4-year all-sky survey is  $\approx 1 \times 10^{-14}\text{ erg cm}^{-2}\text{ s}^{-1}$  in the soft band (0.5–2 keV), which equals the median 0.5–2 keV flux of sample B+C quasars. The 0.5–2 keV fluxes of the 26 X-ray weak quasars in sample B+C range from  $\approx 1 \times 10^{-16}\text{ erg cm}^{-2}\text{ s}^{-1}$  to  $4 \times 10^{-15}\text{ erg cm}^{-2}\text{ s}^{-1}$ , with median and mean values of  $\approx 2 \times 10^{-15}\text{ erg cm}^{-2}\text{ s}^{-1}$ . Thus, the *eROSITA* all-sky survey will probably be unable to enlarge significantly the sample size or unravel the nature of these exceptionally X-ray weak quasars identified here.

We thank the referee for the helpful comments. XP, BL, and HL acknowledge financial support from the National Natural Science Foundation of China grants 11673010 and 11991053, National Key R&D Program of China grant 2016YFA0400702, the Natural Science Foundation of Jiangsu Province (Grant No. BK20150870), and Jiangsu Planned Projects for Postdoctoral Research Funds grant 1601060B. WNB and JDT acknowledge support from NASA ADP grant 80NSSC18K0878, *Chandra* X-ray Center grant G08-19076X, and the V.M. Willaman Endowment.



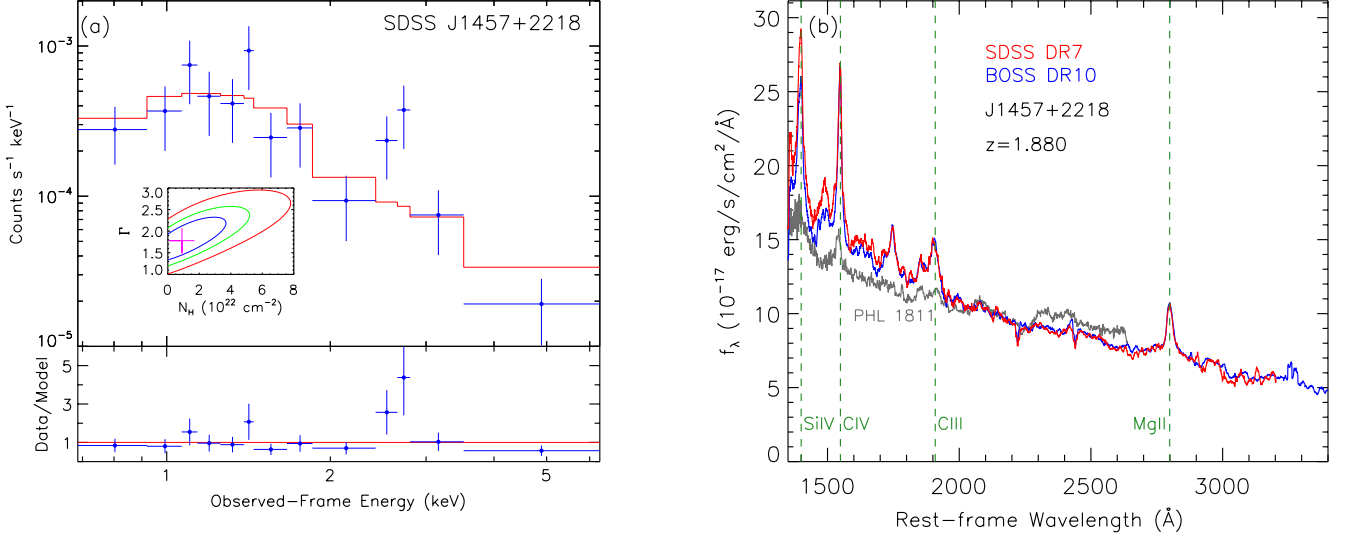


**Figure 10.** (a) *Chandra* broad-band (0.5–7 keV) spectrum of J1457+2218 (blue) and the best-fit model with both Galactic and intrinsic absorption (red). The spectrum was binned to a minimum of five counts per bin for display purposes. The inset shows the best-fit values of  $\Gamma$  and intrinsic  $N_{\text{H}}$  (magenta), and contours of  $\Gamma$  vs.  $N_{\text{H}}$  at confidence levels of 68% (blue), 90% (green), and 99% (red), respectively. The bottom panel is the data divided by the model. (b) SDSS DR7 spectrum (red) and BOSS DR10 spectrum (blue) of J1457+2218. The gray curve shows the PHL 1811 spectrum for comparison.

## APPENDIX

### A. J1457+2218: A CANDIDATE FOR AN INTRINSICALLY X-RAY WEAK QUASAR

One of the WLQs, J1457+2218, is a good candidate for an intrinsically X-ray weak quasar. It has 70 broad-band counts in the source-extraction region: 47 in the soft band and 23 in the hard band, sufficient for basic spectral fitting. Using the CIAO SPECEXTRACT script, we extracted the broad-band spectrum of J1457+2218 from a circular region with a radius of 3.3 pixels centered at the X-ray position, corresponding to a 90% encircled-energy fraction. The background spectrum was extracted from an annular region with an inner radius of 18.3 pixels and an outer radius of 53.3 pixels, which corresponds to the source radius plus 15 and 50 pixels, respectively. Note that J1457+2218 is close to a galaxy cluster, MS 1455.0+2232, which is the target of the *Chandra* observation, and the distance between their centers is 2.0'. Thus, the source and background regions of J1457+2218 are likely to be contaminated by the diffuse source. However, since the photon counts in the background region are relatively uniformly distributed and the spectral counts contain only  $\approx 1$  background count, the nearby galaxy cluster does not affect our spectral analysis significantly.

We performed spectral fitting using XSPEC v12.9.0 (Arnaud 1996). The *C*-statistic (*cstat*) was used given the limited source counts (Cash 1979). We first fit the spectrum with a power-law model modified by only the Galactic absorption (*zpow\*wabs*). The photon index of  $\Gamma = 1.6^{+0.4}_{-0.3}$  derived from this spectral fitting is in agreement with  $\Gamma_{\text{eff}} = 1.6^{+0.3}_{-0.2}$  (Table 6) derived from the band ratio.

We also fit the spectrum with a power-law model modified by both Galactic absorption and intrinsic absorption at the quasar redshift (*zpow\*wabs\*zwabs*). The best-fit values of the photon index and intrinsic absorption column density are  $\Gamma = 1.8^{+0.4}_{-0.3}$  and  $N_{\text{H}} = 0.90^{+1.74}_{-0.89} \times 10^{22} \text{ cm}^{-2}$ , respectively. The errors are quoted at a 68% ( $1\sigma$ ) confidence level. Figure 10(a) shows the X-ray spectrum of J1457+2218 and the best-fit model. We note that there appears to be excess residuals at rest-frame  $\approx 7.6$ –8.1 keV. While the current *Chandra* effective exposure time is 88.4 ks, still deeper X-ray data are required to determine if there is any line emission, which may be due to blueshifted iron emission. It appears that J1457+2218 does not suffer from strong X-ray absorption. J1457+2218 has  $\Delta\alpha_{\text{OX}} = -0.30$ , which corresponds to an X-ray weakness factor of  $f_{\text{weak}} = 6.1$ , and it remains X-ray weak by a factor of 4.7 after

<sup>11</sup> <http://xmmssc.irap.omp.eu/Catalogue/4XMM-DR9/4XMM-DR9.html>

<sup>12</sup> <http://www.mpe.mpg.de/eROSITA>

being corrected for the intrinsic absorption. J1457+2218 is also RI with  $R = 42$  and may have some jet-linked X-ray emission, which would indicate even weaker intrinsic coronal X-ray emission. The spectral fitting results suggest that J1457+2218 is probably an intrinsically X-ray weak WLQ like PHL 1811. Figure 10(b) shows the optical/UV spectra of J1457+2218 and PHL 1811 for comparison. J1457+2218 has overall stronger line emission than PHL 1811; for example, the SDSS (BOSS) C IV REW is 22.0 Å (15.5 Å), while it is 4.7 Å for PHL 1811.

## REFERENCES

- Abazajian, K. N., Adelman-McCarthy, J. K., Agüeros, M. A., et al. 2009, *ApJS*, 182, 543
- Ahn, C. P., Alexandroff, R., Allende Prieto, C., et al. 2014, *ApJS*, 211, 17
- Arnaud, K. A. 1996, in *ASP Conf. Ser.*, Vol. 101, *Astronomical Data Analysis Software and Systems V*, ed. G. H. Jacoby, & J. Barnes (San Francisco:ASP), 17
- Avni, Y., Soltan, A., Tananbaum, H., & Zamorani, G. 1980, *ApJ*, 238, 800
- Avni, Y., & Tananbaum, H. 1982, *ApJL*, 262, L17
- Avni, Y., & Tananbaum, H. 1986, *ApJ*, 305, 83
- Bachev, R., Grupe, D., Boeva, S., et al. 2009, *MNRAS*, 399, 750
- Ballantyne, D. R. 2008, *ApJ*, 685, 787
- Becker, R. H., White, R. L., Helfand, D. J., 1995, *ApJ*, 450, 559
- Blaes, O., Hubeny, I., Agol, E., & Krolik, J. H. 2001, *ApJ*, 563, 560
- Brandt, W. N., Laor, A., & Wills, B. J. 2000, *ApJ*, 528, 637
- Brandt, W. N., & Alexander, D. M. 2015, *A&A Rv*, 23, 1
- Cameron, E. 2011, *PASA*, 665, 1004
- Cardelli, J. A., Clayton, G. C., & Mathis, J. S. 1989, *ApJ*, 345, 245
- Cash, W. 1979, *ApJ*, 228, 939
- Chiaraluce, E., Vagnetti, F., Tombesi, F., & Paolillo, M. 2018, *A&A*, 619, A95
- Condon, J. J., Cotton, W. D., Greisen, E. W., et al. 1998, *AJ*, 115, 1693
- De Cicco, D., Brandt, W. N., Grier, C. J., Paolillo, M., Filiz Ak, N., Schneider, D. P., & Trump, J. R. 2018, *A&A*, 616, A114
- Diamond-Stanic, A. M., Fan, X., Brandt, W. N., et al. 2009, *ApJ*, 699, 782
- Feigelson, E. D., & Nelson, P. I. 1985, *ApJ*, 293, 192
- Freeman, P. E., Kashyap, V., Rosner, R., & Lamb, D. Q. 2002, *ApJS*, 138, 185
- Freeman, P., Doe, S., & Siemiginowska, A. 2001, *Proc. SPIE*, 4477, 76
- Galeev, A. A., Rosner, R., & Vaiana, G. S. 1979, *ApJ*, 229, 318
- Gallagher, S. C., Brandt, W. N., Laor, A., et al. 2001, *ApJ*, 546, 795
- Gallagher, S. C., Brandt, W. N., Chartas, G., & Garmire, G. P. 2002, *ApJ*, 567, 37
- Gallagher, S. C., Brandt, W. N., Chartas, G., et al. 2006, *ApJ*, 644, 709
- Ganguly, R., Bond, N. A., Charlton, J. C., et al. 2001, *ApJ*, 549, 133
- Garmire, G. P., Bautz, M. W., Ford, P. G., Nousek, J. A., & Ricker, Jr., G. R. 2003, *Proc. SPIE*, 4851, 28
- Gallo, L. C., Grupe, D., Schartel, N., et al. 2011, *MNRAS*, 412, 161
- Gehrels, N. 1986, *ApJ*, 303, 336
- Gibson, R. R., Brandt, W. N., & Schneider, D. P. 2008a, *ApJ*, 685, 773
- Gibson, R. R., Brandt, W. N., Schneider, D. P., & Gallagher, S. C. 2008b, *ApJ*, 675, 985
- Gibson, R. R., Jiang, Linhua, Brandt, W. N., et al. 2009a, *ApJ*, 692, 758
- Gibson, R. R., Brandt, W. N., Gallagher, S. C., & Schneider, D. P. 2009b, *ApJ*, 696, 924
- Gibson, R. R., & Brandt, W. N., 2012, *ApJ*, 746, 54
- Green, P. J., & Mathur, S. 1996, *ApJ*, 462, 637
- Hall, P. B., Gallagher, S. C., Richards, G. T., et al. 2006, *AJ*, 132, 1977
- Hewett, P. C., & Wild, V. 2010, *MNRAS*, 405, 2302
- Hickox, R. C., & Alexander, D. M. 2018, *ARA&A*, 56, 625
- Isobe, T., & Feigelson, E. D. 1990, in *BAAS*, 22, 917
- Jiang, L., Fan, X., Ivezić, Ž., Richards, G. T., Schneider, D. P., Strauss, M. A., & Kelly, B. C. 2007, *ApJ*, 656, 680
- Jiang, Y.-F., Stone, J. M., & Davis, S. W. 2014, *ApJ*, 784, 169
- Just, D. W., Brandt, W. N., Shemmer, O., et al. 2007, *ApJ*, 665, 1004
- Koratkar, A., & Blaes, O., 1999, *PASP*, 111, 1
- Kraft, R. P., Burrows, D. N., & Nousek, J. A. 1991, *ApJ*, 374, 344
- Krawczyk, C. M., Richards, G. T., Gallagher, S. C., et al. 2015, *AJ*, 149, 203
- Lacy, M., Baum, S. A., Chandler, C. J., et al. 2019, *arXiv:1907.01981*
- Lacy, M., Gates, E., Brandt, W., et al. 2020, in *BAAS*, 52, No. 1
- LaMassa, S. M., Cales, S., Moran, E. C., et al. 2015, *ApJ*, 800, 144

- Laor, A., & Davis, S. W., 2011, MNRAS, 417, 681
- LaValley, M., Isobe, T., & Feigelson, E. 1992, in  
Astronomical Society of the Pacific Conference Series,  
Vol. 25, Astronomical Data Analysis Software and  
Systems I, ed. D. M. Worrall, C. Biemesderfer, &  
J. Barnes, 245
- Leighly, K. M., Halpern, J. P., Jenkins, E. B., & Casebeer,  
D. 2007a, ApJS, 173, 1
- Leighly, K. M., Halpern, J. P., Jenkins, E. B., et al. 2007b,  
ApJ, 663, 103
- Liu, H., Luo, B., Brandt, W. N., et al. 2018, ApJ, 859, 113
- Liu, H., Luo, B., Brandt, W. N., et al. 2019, ApJ, 878, 79
- Luo, B., Brandt, W. N., Alexander, D. M., et al. 2013, ApJ,  
772, 153
- Luo, B., Brandt, W. N., Alexander, D. M., et al. 2014, ApJ,  
794, 70
- Luo, B., Brandt, W. N., Hall, P. B., et al. 2015, ApJ, 805,  
122
- Luo, B., Brandt, W. N., Xue, Y. Q., et al. 2017, ApJS, 228,  
2
- Lusso, E., Comastri, A., Vignali, C., et al. 2010, A&A, 512,  
A34
- Lusso, E., & Risaliti, G. 2016, ApJ, 819, 154
- Lyke, B. W., Higley, A. N., McLane, J. N., et al. 2020  
ApJS, in press
- Marconi, A., Axon, D. J., Maiolino, R., et al. 2008, ApJ,  
678, 693
- Marconi, A., Axon, D. J., Maiolino, R., et al. 2009, ApJL,  
698, L103
- Margala, D., Kirkby, D., Dawson, K., et al. 2016, ApJ, 831,  
157
- Markwardt, C. B. 2009, Astronomical Data Analysis  
Software and Systems XVIII, 411, 251
- McGraw, S. M., Brandt, W. N., Grier, C. J., et al. 2017,  
MNRAS, 469, 3163
- Merloni, A., Predehl, P., Becker, W., et al. 2012,  
arXiv:1209.3114
- Miller, B. P., Brandt, W. N., Schneider, D. P., et al. 2011,  
ApJ, 726, 20
- Miniutti, G., Brandt, W. N., Schneider, D. P., et al. 2012,  
MNRAS, 425, 1718
- Nardini, E., Lusso, E., Risaliti, G., et al. 2019, A&A, 632,  
A109
- Netzer, H., & Marziani, P. 2010, ApJ, 724, 318
- Netzer, H., & Trakhtenbrot, B. 2014, MNRAS, 438, 672
- Ni, Q., Brandt, W. N., Luo, B., et al. 2018, MNRAS, 480,  
5184
- Ni, Q., Brandt, W. N., Yi, W., et al. 2020, ApJL, 889, L37
- O'Donnell, J. E. 1994, ApJ, 422, 158
- Pâris, I., Petitjean, P., Aubourg, É., et al. 2012, A&A, 548,  
A66
- Pâris, I., Petitjean, P., Aubourg, É., et al. 2014, A&A, 563,  
A54
- Park, T., Kashyap, V. L., Siemiginowska, A., et al. 2006,  
ApJ, 652, 610
- Pei, Y. C. 1992, ApJ, 395, 130
- Plotkin, R. M., Anderson, S. F., Brandt, W. N., et al.  
2010a, ApJ, 721, 562
- Plotkin, R. M., Anderson, S. F., Brandt, W. N., et al.  
2010b, AJ, 139, 390
- Reeves, J. N., Turner, M. J. L., Ohashi, T., & Kii, T. 1997,  
MNRAS, 292, 468
- Reynolds, C. S., & Nowak, M. A. 2003, PhR, 377, 389
- Reichard, T. A., et al. 2003, AJ, 126, 2594
- Richards, G. T., et al. 2001, AJ, 121, 2308
- Richards, G. T., et al. 2003, AJ, 126, 1131
- Richards, G. T., Strauss, M. A., Fan, X., et al. 2006, AJ,  
131, 2766
- Rogerson, J. A., Hall, P. B., Ahmed, N. S., Hidalgo, P. R.,  
Brandt, W. N., & Filiz Ak, N. 2018, ApJ, 862, 22
- Rosen, S. R., et al. 2016, A&A, 590, A1
- Sameer, Brandt, W. N., Anderson, S., et al. 2019, MNRAS,  
482, 1121
- Schneider, D. P., Richards, G. T., Hall, P. B., et al. 2010,  
AJ, 139, 2360
- Shemmer, O., Brandt, W. N., Anderson, S. F., et al. 2009,  
ApJ, 696, 580
- Shen, Y., Richards, G. T., Strauss, M. A., et al. 2011,  
ApJS, 194, 45
- Slone, O., & Netzer, H. 2012, ApJ, 426, 656
- Spergel, D. N., et al. 2007, ApJS, 170, 377
- Steffen, A. T., Strateva, I., Brandt, W. N., et al. 2006, AJ,  
131, 2826
- Stoche 1992, J. T., Morris, S. L., Weymann, R. J., & Foltz,  
C. B. 1992, ApJ, 396, 487
- Strateva, I. V., Brandt, W. N., Schneider, D. P., Vanden  
Berk, D. G., & Vignali, C. 2005, AJ, 130, 387
- Tananbaum, H., et al. 1979, ApJL, 234, L9
- Timlin, J. D., Brandt, W. N., Ni, Q., Luo, B., Pu, X.,  
Schneider, D. P., Vivek, M., Yi, W. 2020, MNRAS, 492,  
719
- Thompson, T. A., Quataert, E., & Murray, N. 2005, ApJ,  
630, 167
- Trump, J. R., et al. 2006, ApJS, 165, 1
- Vanden Berk, D. E., et al. 2001, AJ, 122, 549
- Vestergaard, M., & Osmer, P. S. 2009, ApJ, 699, 800
- Vestergaard, M., & Peterson, B. M. 2006, ApJ, 641, 689
- Vignali, C., Brandt, W. N., Schneider, D. P. 2003, AJ, 125,  
433

- Watson, M. G., et al. 2009, *A&A*, 493, 339
- Weymann, R. J., Morris, S. L., Foltz, C. B., & Hewett, P. C. 1991, *ApJ*, 373, 23
- White, R. L., Becker, R. H., Helfand, D. J., & Gregg, M. D. 1997, *ApJ*, 475, 479
- Wilkes, B. J., Tananbaum, H., Worrall, D. M., Avni, Y., Oey, M. S., & Flanagan, J. 1994, *ApJS*, 92, 53
- Wilkes, B. J., Bounds, K. A., Schmidt, G. D., et al. 2005, *ApJ*, 634, 183
- Worrall, D. M., Tananbaum, H., Giommi, P., & Zamorani, G. 1987, *ApJ*, 313, 596
- Wu, J., Brandt, W. N., Comins, M. L., et al. 2010, *ApJ*, 724, 762
- Wu, J., Brandt, W. N., Hall, P. B., et al. 2011, *ApJ*, 736, 28
- Wu, J., Brandt, W. N., Anderson, S. F., et al. 2012, *ApJ*, 747, 10
- Xue, Y. Q., Luo, B., Brandt, W. N., et al. 2011, *ApJS*, 195, 10
- Yang, G., Brandt, W. N., Luo, B., et al. 2016, *ApJ*, 831, 145
- York, D. G., Adelman, J., Anderson, Jr., J. E., et al. 2000, *AJ*, 120, 1579
- Zamorani, G., et al. 1981, *ApJ*, 245, 357
- Zappacosta, L., Piconcelli, E., Giustini, M., et al. 2020, *A&A*, 635, L5
- Zhu, S. F., Brandt, W. N., Luo, B., et al. 2020, *MNRAS*, 496, 245